Journal of Computational Physics 229 (2010) 7715–7738

Contents lists available at ScienceDirect

Journal of Computational Physics

journal homepage: www.elsevier.com/locate/jcp

A wavelet-based multiresolution approach to large-eddy simulation of turbulence

M. de la Llave Plata *, R.S. Cant

Engineering Department, University of Cambridge, Trumpington Street, CB2 1PZ Cambridge, UK

ARTICLE INFO

Article history:
Received 10 January 2008
Received in revised form 27 April 2010
Accepted 16 June 2010
Available online 25 June 2010

Keywords:
Large-eddy simulation
Multiscale methods
Multiresolution analysis
Wavelets

ABSTRACT

The wavelet-based multiresolution analysis (MRA) technique is used to develop a modelling approach to large-eddy simulation (LES) and its associated subgrid closure problem. The LES equations are derived by projecting the Navier–Stokes (N–S) equations onto a hierarchy of wavelet spaces. A numerical framework is then developed for the solution of the large and the small-scale equations. This is done in one dimension, for the Burgers equation, and in three dimensions, for the N–S problem. The proposed methodology is assessed in *a priori* tests on an atmospheric turbulent time series and on data from direct numerical simulation. *A posteriori* (dynamic) tests are also carried out for decaying and force-driven Burgers turbulence.

1. Introduction

The numerical simulation of turbulent flows is a topic of acknowledged practical importance to scientists and engineers. Due to the wide range of length and time scales involved in turbulence, direct numerical simulation (DNS) of turbulent flows is computationally very expensive, and is restricted to low-to-moderate Reynolds numbers. The LES technique has been established as an alternative approach to DNS for high-Reynolds-number flows. The ultimate goal of LES is to compute explicitly the large-scale motion, while modelling the effect of the small scales on the coarse resolved field.

In order to obtain accurate solutions of the LES equations, it is essential to develop modelling approaches able to capture the main features of the interscale dynamics. Multilevel LES methods accomplish this by simulating the most relevant part of these dynamics explicitly in the computational domain. They rely on the decomposition of the flow into different frequency bands, each associated with a particular range of length scales. The multiscale decomposition of the flow is usually achieved in either of the following ways:

(1) Some methods are based on the implementation of multigrid-type prolongation and restriction operators, which permit the exchange of information between the hierarchy of grids involved in the simulation. This category includes the multiple mesh simulation (MMS) method developed by Voke [1,2], the multilevel LES approach proposed by Terracol et al. [3,4], and the modified subgrid-scale (SGS) estimation model of Domaradzki and Yee [5].
(2) Other methods resort to the projection of the flow equations onto a set of orthogonal basis functions, such as Fourier spectral methods or Galerkin-type methods. These methods are related to the multiscale decomposition framework or similar methods such as the additive turbulent decomposition (ATD) approach originally proposed by McDonough et al. [6,7]. In the context of LES, Hughes et al. have developed the variational multiscale simulation (VMS) method

* Corresponding author. Present address: ONERA, The French Aerospace Lab, BP 72 – 92322 Châtillon, France. Tel.: +33 1 46 73 42 23; fax: +33 1 46 73 41 66.
E-mail address: mllave@onera.fr (M. de la Llave Plata).

0021-9991/$ - see front matter © 2010 Elsevier Inc. All rights reserved.
doi:10.1016/j.jcp.2010.06.027

[8,9], which is based on a variational projection of the N–S equations instead of spatial filtering, as is done in conventional LES.

At this point, it appears natural to introduce the concept of wavelet-based MRA as an attractive alternative to the decomposition methods outlined above. Indeed, the locality property of the wavelet transform (WT), together with its resolution adaptability, and most importantly, its ability to preserve the scale-invariance properties of the analysed signal, makes it a very appealing tool for LES subgrid modelling.

The use of wavelets for the numerical solution of flows dates back to the work of Liandrat and Tchamitchian [10] and Bacry et al. [11]. New approaches to study and model turbulent flows using the wavelet representation have been investigated by Meneveau [12] and Farge [13]. Based on wavelet thresholding, Farge et al. [14] have proposed the coherent vortex simulation (CVS) technique, which permits the separation of a flow into coherent (organised) and incoherent (random noise) structures. Wavelet-based methods for the solution of turbulent reacting flows have also been developed by Prosser and Cant [15] and Bockhorn et al. [16]. In the context of LES, Goldstein and Vasilyev [17] and Goldstein et al. [18] have recently proposed the stochastic coherent adaptive large-eddy simulation (SCALES) technique, which combines CVS filtering with the Germano dynamic approach [19].

The main goal of this research is therefore to exploit the qualities of the WT, in order to develop a multilevel LES approach, based on the MRA technique.

In order to derive a system of equations for the large and the small scales, the N–S equations are projected onto a hierarchy of scaling function (coarse grid) and wavelet spaces (fine grids) at different levels of resolution. The set of equations which results from this projection describes the evolution of the scaling function coefficients (large scales) and the wavelet coefficients (small scales) directly in the wavelet domain. This approach shares some similarities with the VMS framework [8,9], with the difference that the wavelet-based LES equations presented here are formulated in the strong sense, in contrast to VMS which rests on a weak formulation of the N–S problem. Indeed, the selected wavelet basis provides a finite-difference (FD) framework for the discretisation of the spatial derivatives in the equations. The differential operator is expressed, in the transform domain, in terms of a hierarchy of sub-operators which represent the interactions between wavelet components across scales. The accuracy of the FD approximation is determined by the properties of the basis functions. The gain in computational efficiency with respect to DNS is achieved by truncating the wavelet expansion of the solution at a prescribed level. The small-scale equations can thus be understood as a projection of the N–S system on a truncated hierarchy of wavelet spaces. The subgrid terms which arise from the projection of the N–S equations on the coarsest grid (LES grid) are then approximated using the available small-scale information. The reconstruction and projection operators which permit the communication between computational grids are now readily provided by the WT algorithm. A major advantage of this approach is the fact that wavelet-based discretisations offer a natural environment for the implementation of adaptive schemes, such as that used in SCALES [17,18]. This is specially useful in problems where strong inhomogeneities exist in the flow (boundary layers, shear layers, etc.). Furthermore, the wavelet-based framework proposed in this research sidesteps the difficulties associated with the modelling of commutation errors, since the subgrid and the truncation error terms which result from the projection of the equations are treated jointly.

This paper is organised as follows. Section 2 presents a brief overview of the MRA technique in the context of the orthogonal WT. The notation used throughout this paper is introduced in Section 3. Section 4 lays out the key steps in the development of our wavelet-based approach as an effective strategy for LES subgrid modelling. The LES equations are derived and a numerical framework for their solution is developed in one and three dimensions. Results from *a priori* tests of the methodology on a turbulent time series from experiment and on DNS data are reported in Section 5. The outcome of *a posteriori* tests performed on the Burgers equation are then discussed in Section 6. Finally, Section 7 presents the main conclusions from this research and offers a set of recommendations for future work.

2. Wavelet-based multiresolution analysis

The principle of MRA, introduced by Mallat [20], is to analyse the data at different scale and space resolutions, viewing the signal through windows of different sizes. Large windows will capture the global behaviour, whereas small windows will focus on local features. The MRA can thus be interpreted as a decomposition into approximations at coarser and coarser resolutions. The details, which have been lost when moving from a higher level of approximation to a lower one, are encoded in the wavelet coefficients.

An MRA of $\mathbf{L}^2(\mathbb{R})$ is defined by a sequence of nested spaces $\{\mathbf{V}_j\}_{j\in\mathbb{Z}}$,

$$\{0\} \subset \cdots \subset \mathbf{V}_{j-1} \subset \mathbf{V}_j \subset \mathbf{V}_{j+1} \subset \cdots \subset \mathbf{L}^2(\mathbb{R}) \tag{1}$$

For each subspace, there exists a function $\phi_{j,k}(x) \in \mathbf{V}_j$, called a *scaling function*, which can be obtained by translation and dilation of a *mother scaling function*, $\phi(x) \in \mathbf{L}^2(\mathbb{R})$, as $\phi_{j,k}(x) = \phi(2^j x - k)$. Here $j, k \in \mathbb{Z}$ are the scale and position indices, respectively.

The projection $P_j(f)$, of a signal $f(x) \in \mathbf{L}^2(\mathbb{R})$ on a subspace $\mathbf{V}_j$, is expressed in terms of the *scaling function coefficients*, $s_{j,k}$, defined by the inner products between the signal and the scaling functions,

$$P_j(f) = \sum_{k=1}^{2^j} s_{j,k}\phi_{j,k}(x), \quad s_{j,k} = \langle f(u), \phi_{j,k}(u)\rangle \tag{2}$$

The detail information required to move up one resolution level is contained in the complement space of $\mathbf{V}_j$, namely $\mathbf{W}_j$, such that, $\mathbf{V}_j \oplus \mathbf{W}_j = \mathbf{V}_{j+1}$. The subspaces $\mathbf{W}_j$ are called *wavelet spaces*. If the wavelet basis is orthogonal, then $\mathbf{V}_j$ and $\mathbf{W}_j$ possess the following properties,

$$\mathbf{V}_j \perp \mathbf{W}_j, \quad \mathbf{W}_m \perp \mathbf{W}_n \quad \forall m \neq n \tag{3}$$

The projection $Q_j(f)$, of $f(x)$ on $\mathbf{W}_j$, is written in terms of the *wavelet coefficients*, $d_{j,k}$, defined by the inner products between the signal and the *wavelet functions*, $\psi_{j,k}(x) \in \mathbf{W}_j$,

$$Q_j(f) = \sum_{k=1}^{2^j} d_{j,k}\psi_{j,k}(x), \quad d_{j,k} = \langle f(u), \psi_{j,k}(u)\rangle \tag{4}$$

As with the scaling functions, the wavelets are dilations and translations of a *mother wavelet*, $\psi(x) \in \mathbf{L}^2(\mathbb{R}) : \psi_{j,k}(x) = \psi(2^j x - k)$.

The MRA representation of a signal $f(x)$ can therefore be written in terms of a hierarchy of scaling function and wavelet spaces as

$$f(x) = P_0(f) + \sum_{i=0}^{\infty} Q_i(f) = \sum_k s_{0,k}\phi_{0,k}(x) + \sum_{i,m} d_{i,m}\psi_{i,m}(x) \tag{5}$$

In three dimensions (3D), it is possible to define an MRA of $\mathbf{L}^2(\mathbb{R}^3)$ by defining a new separable basis as the tensor product of one-dimensional (1D) scaling functions and wavelets in each of the axis directions. In a 3D domain, the MRA of a function $f(\mathbf{x}) \in \mathbf{L}^2(\mathbb{R}^3)$ is thus given at each resolution level i by its projection on a scaling function space, $\mathbf{V}_i^3 = \mathbf{V}_i^{(x)} \otimes \mathbf{V}_i^{(y)} \otimes \mathbf{V}_i^{(z)}$, with associated basis functions $\phi_{i,k_x}(x)\phi_{i,k_y}(y)\phi_{i,k_z}(z)$, and on seven wavelet spaces $\{\mathbf{W}_i^{(r)}\}_{r=1,\ldots,7}$, namely,

$$\begin{aligned}
\mathbf{W}_i^{(1)} &= \mathbf{W}_i^{(x)} \otimes \mathbf{V}_i^{(y)} \otimes \mathbf{V}_i^{(z)} \\
\mathbf{W}_i^{(2)} &= \mathbf{V}_i^{(x)} \otimes \mathbf{W}_i^{(y)} \otimes \mathbf{V}_i^{(z)} \\
\mathbf{W}_i^{(3)} &= \mathbf{V}_i^{(x)} \otimes \mathbf{V}_i^{(y)} \otimes \mathbf{W}_i^{(z)} \\
\mathbf{W}_i^{(4)} &= \mathbf{W}_i^{(x)} \otimes \mathbf{W}_i^{(y)} \otimes \mathbf{V}_i^{(z)} \\
\mathbf{W}_i^{(5)} &= \mathbf{W}_i^{(x)} \otimes \mathbf{V}_i^{(y)} \otimes \mathbf{W}_i^{(z)} \\
\mathbf{W}_i^{(6)} &= \mathbf{V}_i^{(x)} \otimes \mathbf{W}_i^{(y)} \otimes \mathbf{W}_i^{(z)} \\
\mathbf{W}_i^{(7)} &= \mathbf{W}_i^{(x)} \otimes \mathbf{W}_i^{(y)} \otimes \mathbf{W}_i^{(z)}
\end{aligned}$$

with associated wavelet functions given by the product of the basis functions of the constituent 1D spaces. The superscript r is called the orientation index. For instance, the 3D wavelet function associated with the wavelet space $\mathbf{W}_i^{(4)}$ is $\psi_{i,m_x}(x)\psi_{i,m_y}(y)\phi_{i,m_z}(z)$. See [21] for more details on multidimensional MRA.

2.1. Selected wavelet basis

The orthogonal wavelet family proposed by Daubechies [22] has been selected as basis for the wavelet-based LES technique developed in the following sections. They are characterised by having compact support, and the highest number of vanishing moments compatible with their support width. The compact support property is essential in order to achieve sparse representations of the analysed signals. It is also needed to obtain compact finite difference schemes for the discretisation of the derivatives in the flow equations. Since the N–S equations contain derivatives up to order two, wavelets are required which are at least twice differentiable. The wavelet family with narrowest support width to fulfil this condition is the Daubechies six-tap filter (*Daub 6*). This family is defined by six filter coefficients and has three vanishing moments. The approximation of the first derivative in this basis leads to a sixth-order accurate FD scheme.

3. A word on notation

The notation used throughout this work is essentially similar to that used by Beylkin and Keiser [23].

3.1. Notation in 1D

3.1.1. Projection

Any variable $f(x) \in \mathbf{L}^2(\mathbb{R})$ can be approximated by its discrete representation in a sufficiently high resolution space $\mathbf{V}_J$,

$$f(x) \approx P_J(f) = \sum_{k=1}^{2^J} f_k\phi_{J,k}(x) \tag{6}$$

defined by 2^J sample values. A coarser representation of f is then given by its projection, $P_j(f)$, onto the scaling function space $\mathbf{V}_j$, defined by 2^j scaling function coefficients, with $j < J$. In the context of LES, we will associate the coarse space, $\mathbf{V}_j$, with the LES grid, whose size is $\Delta_{LES} = 2^{-j}$. The full resolution space $\mathbf{V}_J$ is thus equivalent to the DNS field, with grid spacing $\Delta_{DNS} = 2^{-J}$. Hence, the approximations $P_j(f)$ and $P_J(f)$, or in shorthand notation f_j and f_J, will correspond to the LES and DNS flow solutions respectively. To reconstruct $P_J(f)$ from $P_j(f)$ we must add the details contained in the wavelet spaces, $\{Q_j(f) + Q_{j+1}(f) + \cdots + Q_{J-1}(f)\}$. For compactness, these terms will be grouped under $Q_{j,SGS}(f)$ (in shorthand form f'_j), which encompass the unknown subgrid scales. Using this notation, a variable $f(x)$ can be decomposed into its resolved and subgrid components as

$$f(x) \approx P_J(f) = P_j(f) + \sum_{i=j}^{J-1} Q_i(f) = P_j(f) + Q_{j,SGS}(f) = f_j + f'_j \tag{7}$$

3.1.2. Reconstruction

The symbol $\mathcal{R}_{j_1}^{j_2}[\cdot]$ will designate the operator to reconstruct, or represent, a vector on subspace $\mathbf{V}_{j_1}$ or $\mathbf{W}_{j_1}$, in the subspace $\mathbf{V}_{j_2}$, with $j_2 > j_1$. On $\mathbf{V}_{j_2}$ one can then use the coefficients of $\mathcal{R}_{j_1}^{j_2}[P_{j_1}(f)]$ and $\mathcal{R}_{j_1}^{j_2}[Q_{j_1}(f)]$ to perform the pertinent operations. When the level of origin, j_1, and destination, j_2, are the same, the superscript is dropped and the operator $\mathcal{R}_{j_1}[P_{j_1}(f)]$ simply represents the scaling function coefficients of the projection of f on $\mathbf{V}_{j_1}$. The purpose of including the new operator $\mathcal{R}_{j_1}[\cdot]$ in the formulation is to draw a distinction between $P_{j_1}(u)^2$ and $\mathcal{R}_{j_1}[P_{j_1}(u)]^2$. The former is equivalent to $\mathcal{R}_{j_1}^{J}[P_{j_1}(u)]^2$, which amounts to reconstructing $P_{j_1}(u)$ in $\mathbf{V}_J$, then using ordinary multiplication to evaluate $P_{j_1}(u)^2$. The outcome of this is a vector which lives in $\mathbf{V}_J$ and (possibly) spans across all resolutions. By contrast, calculating $\mathcal{R}_{j_1}[P_{j_1}(u)]^2$ simply implies taking the pointwise product of the scaling function coefficients of $P_{j_1}(u)$ which now remain in $\mathbf{V}_{j_1}$. This notation will be of use in the evaluation of the non-linear terms in the LES equations.

3.1.3. Differential operator

The operators $(P_j\,\partial/\partial x, P_j\partial^2/\partial x^2)$ will represent the FD approximations on $\mathbf{V}_j$ of the first and second derivatives, respectively. Similarly, the operators $(Q_i\partial/\partial x, Q_i\partial^2/\partial x^2)$ will represent the FD approximations of the first and second derivatives on $\mathbf{W}_i$. In a more abbreviated form, $P_j\partial/\partial x$ and $P_j\partial^2/\partial x^2$ will be also written as $\partial_j^{(1)}$ and $\partial_j^{(11)}$, respectively, where the superscript "1" indicates that the derivatives are taken with respect to the first coordinate direction x.

3.2. Notation in 3D

3.2.1. Projection

When referring to the scaling function spaces, or their projection operators, we add the superscript "3", e.g. $\mathbf{V}_j^3$ and $P_j^3(\cdot)$. The projection on a generic wavelet space $\mathbf{W}_i^{(r)}$ is now denoted by $Q_i^{(r)}(\cdot)$. The LES and DNS grids are defined by $\mathbf{V}_j^3$ and $\mathbf{V}_J^3$, respectively, and have mesh sizes $\Delta_{LES} = 2^{-3j}$ and $\Delta_{DNS} = 2^{-3J}$. The associated LES and DNS solutions for a flow variable $f(\mathbf{x}) \in \mathbf{L}^2(\mathbb{R}^3)$ are $P_j^3(f)$ (or equivalently, f_j) and $P_J^3(f)$ (equivalently, f_J), respectively. The subgrid terms, given by the differences $\left\{P_J^3(f) - P_j^3(f)\right\}$, are grouped under $Q_{j,SGS}^3(f)$ (in shorthand f'_j). The MRA decomposition of $f(\mathbf{x})$ can therefore be expressed as

$$f(\mathbf{x}) \approx P_J^3(f) = P_j^3(f) + \sum_{i=j}^{J-1}\sum_{r=1}^{7} Q_i^{(r)}(f) = P_j^3(f) + Q_{j,SGS}^3(f) = f_j + f'_j \tag{8}$$

which splits $f(\mathbf{x})$ into its resolved and subgrid components.

3.2.2. Reconstruction

In a 3D framework, $\mathcal{R}_{j_1}^{j_2}[\cdot]$ is the prolongation operator which reconstructs a vector on $\mathbf{V}_{j_1}^3$ in the higher resolution space $\mathbf{V}_{j_2}^3 (j_2 > j_1)$. As in 1D, $\mathcal{R}_{j_1}\left[P_{j_1}^3(f)\right]$ represents the scaling function coefficients of $P_{j_1}^3(f)$, i.e. the coefficients of the projection of f on $\mathbf{V}_{j_1}^3$.

3.2.3. Differential operator

The difference operators $\left(P_j^3\partial/\partial x_k, P_j^3\partial^2/\partial x_k^2\right)$ and $\left(Q_i^{(r)}\partial/\partial x_k, Q_i^{(r)}\partial^2/\partial x_k^2\right)$ represent the FD approximations on $\mathbf{V}_j$ and $\mathbf{W}_i^{(r)}$, respectively, of the first and second derivatives in the x_k-axis direction. By analogy with the 1D problem, $\left(\partial_j^{(k)}, \partial_j^{(kk)}\right)$ is the shorthand notation for $\left(P_j^3\partial/\partial x_k, P_j^3\partial^2/\partial x_k^2\right)$.

4. Wavelet-based large-eddy simulation

The wavelet-based LES approach proposed herein is firstly illustrated for the Burgers equation, which produces a 1D analogue of the turbulent energy cascade. This simplified system allows the derivation of a schematic multiresolution represen-

tation of the LES equations, avoiding the cumbersome notation of the full 3D problem. The extrapolation of the methodology to 3D is presented in Section 4.4.

4.1. Burgers equation in wavelet bases

The non-dimensional Burgers equation in physical space reads

$$\frac{\partial u}{\partial t}+\frac{\partial}{\partial x}\left(\frac{u^2}{2}\right)-\frac{1}{Re}\frac{\partial^2 u}{\partial x^2}=0 \tag{9}$$

where Re is the Burgers equivalent of the Reynolds number, defined in terms of characteristic quantities of the problem. If we project (9) onto the LES grid, $\mathbf{V}_j$, and reunite the resolved terms on the left-hand side (l.h.s.), we obtain

$$\frac{\partial}{\partial t}P_j(u)+\frac{1}{2}P_j\frac{\partial}{\partial x}P_j(u)^2-\frac{1}{Re}P_j\frac{\partial^2}{\partial x^2}P_j(u)=-\frac{1}{2}P_j\frac{\partial}{\partial x}\left(u^2-P_j(u)^2\right)+\frac{1}{Re}P_j\frac{\partial^2}{\partial x^2}(u-P_j(u)) \tag{10}$$

The first term on the right-hand side (r.h.s.) of (10) is called the *convective SGS term*. It will be denoted by $\partial_j^{(1)}\mathcal{C}_j$, where $\mathcal{C}_j=\left(u^2-P_j(u)^2\right)$, and $\partial_j^{(1)}$ is the differential operator defined in Section 3.1. The nature of this term can be brought out by making use of (7), namely,

$$\partial_j^{(1)}\mathcal{C}_j=\frac{1}{2}P_j\frac{\partial}{\partial x}(P_J(u)-P_j(u))(P_J(u)+P_j(u))=\frac{1}{2}P_j\frac{\partial}{\partial x}\left(2P_j(u)Q_{j,SGS}(u)+Q_{j,SGS}(u)^2\right) \tag{11}$$

The expansion (11) highlights the existence of two distinct contributions. The first one is due to interactions between the resolved (RES) and the subgrid scales (SGS). It will be identified as the RES–SGS component. The second one represents the interactions only between the subgrid scales. It will be called the SGS–SGS component. Note that, unlike conventional LES, commutation between the projection and derivative operators is not assumed. This will generate an additional *viscous SGS term*, second element on the r.h.s. of (10). This new term will be denoted by $\partial_j^{(11)}\mathcal{D}_j$, where $\mathcal{D}_j=1/Re(u-P_j(u))$, and $\partial_j^{(11)}$ was defined in Section 3.1,

$$\partial_j^{(11)}\mathcal{D}_j=\frac{1}{Re}P_j\frac{\partial^2}{\partial x^2}(P_J(u)-P_j(u))=\frac{1}{Re}P_j\frac{\partial^2}{\partial x^2}Q_{j,SGS}(u) \tag{12}$$

4.2. Modelling approach

The modelling strategy used in this research starts with the observation that, if the flow field has a Kolmogorov-like spectrum, $\kappa^{-\beta}$, and if the wavelet basis has sufficient regularity (fast decay of the wavelet coefficients and of the wavelet derivatives), a good representation of the subgrid-scale field is given by the M first terms in the wavelet series. For an M-level approach, this means:

$$Q_{j,SGS}(u)\approx Q_j(u)+Q_{j+1}(u)+\cdots+Q_{j+M-1}(u) \tag{13}$$

The evolution of each wavelet component is governed by the projection of (9) onto the subspaces $\mathbf{W}_m$, $m=j,\ldots,j+M-1$,

$$\frac{\partial}{\partial t}Q_m(u)+\frac{1}{2}Q_m\frac{\partial}{\partial x}u^2-\frac{1}{Re}Q_m\frac{\partial^2}{\partial x^2}u=0 \tag{14}$$

Invoking the assumptions made above, the full resolution field, u, may be approximated by the sum of the resolved field and the leading terms in the expansion (13), namely,

$$u\approx P_j(u)+Q_j(u)+\cdots+Q_{j+M-1}(u)=P_{j+M}(u) \tag{15}$$

Substituting (15) into (14) yields

$$\frac{\partial}{\partial t}Q_m(u)+\frac{1}{2}Q_m\frac{\partial}{\partial x}P_{j+M}(u)^2-\frac{1}{Re}Q_m\frac{\partial^2}{\partial x^2}P_{j+M}(u)=0 \tag{16}$$

where the index m spans from j to $j+M-1$. Eqs. (10) and (16) constitute a system of $M+1$ coupled equations for the resolved (or large scale) and the subgrid (or small-scale) fields.[1]

Observe that, in the DNS limiting case, the number of levels considered in the simulation is $M=J-j$, and all the wavelet coefficients, down to the Kolmogorov scale $\left(\eta\sim 2\Delta_{DNS}=1/2^{J-1}\right)$, are computed explicitly.

[1] Throughout this work, we will refer to the wavelet coefficients as subgrid scales or small scales, synonymously. By subgrid, we mean that these scales are defined on a grid which is finer than the LES grid $\mathbf{V}_j$. In contrast to the scaling function coefficients, representative of the large scales, which are *well resolved* on $\mathbf{V}_j$, the subgrid field provided by the solution of (16) has been approximated using a *truncated* wavelet expansion, and therefore it is *under-resolved*.

4.3. Practical implementation in 1D

This section deals with the practical implementation of our wavelet-based LES technique. For simplicity, we assume that the equations are solved by means of an explicit Euler method for time advancement. The way in which the formulation is presented in this research leaves the way open to the implementation of more advanced algorithms.

The estimation of the subgrid-scale field from (16) requires the definition of a hierarchy of grids with sizes $\Delta_m = 2^{-m}$. Each of these grids will be associated with a wavelet space $\mathbf{W}_m$. This leads to a multilevel approach in which the number of levels is prescribed by the number of terms considered in the series (13). We now proceed to explain how (10) and (16) are solved numerically.

4.3.1. Resolved non-linear term

Taking the square of the resolved field, $P_j(u)^2$, will generate new coefficients over a range of wavelet spaces. Most of the traditional LES approaches fail to take this into account, and are mathematically inconsistent in this regard [24–26]. This is because the filtered advective term $\overline{\bar{u}_k\bar{u}_l}$ is replaced in the equations by $(\bar{u}_k\bar{u}_l + \tau_{kl})$. Yet, the spectral content of the product of two grid-filtered quantities, $\bar{u}_k\bar{u}_l$, is larger than the maximum wavenumber that can be represented on the LES grid. These unrepresented high-frequency modes can alias back to the resolved field and interfere with the dynamics of the turbulence over a broad range of scales [25]. Nevertheless, we would expect the extent of these contributions to be limited to spaces in the vicinity of $\mathbf{V}_j$. This turned out to be the case for the turbulence data analysed in this work. Clearly, the spread of the product will depend on the nature of the signal under study. However, for smooth solutions of the N–S equations a good approximation is

$$P_j\frac{\partial}{\partial x}P_j(u)^2 \approx P_j\frac{\partial}{\partial x}\mathcal{R}_j^{j+1}\left[P_j(u)\right]^2 \tag{17}$$

which amounts to reconstructing $P_j(u)$ in $\mathbf{V}_{j+1}$, taking the pointwise product of the coefficients $\mathcal{R}_j^{j+1}[P_j(u)]^2$, and applying the differential operator $\partial_j^{(1)}$ to the resulting field. An in-depth discussion on the treatment of non-linearities in wavelet bases can be found in [23].

4.3.2. Closure terms

Inference of the small-scale field requires the evaluation of the wavelet coefficients at the prescribed number of levels, whose temporal evolution is governed by (16). An initial state must also be prescribed. The initial wavelet field may be set to zero, or obtained by performing an MRA of available DNS data.

At a generic level m, the wavelet coefficients can be calculated from

$$Q_m(u)^{n+1} = Q_m(u)^n + \Delta t\left\{-\frac{1}{2}Q_m\frac{\partial}{\partial x}\mathcal{R}_{j+M}[P_{j+M}(u)]^2 + \frac{1}{Re}Q_m\frac{\partial^2}{\partial x^2}P_{j+M}(u)\right\} \tag{18}$$

where Δt is the time step and the superscript n refers to the solution at time $t_n = n\Delta t$. The approximation $P_{j+M}(u)$ is defined on the finest grid considered in the simulation,

$$\mathbf{V}_{j+M} = \mathbf{V}_j \overset{j+M-1}{\underset{i=j}{\oplus}} \mathbf{W}_i \tag{19}$$

and can be calculated from the most recent available information in the computation, namely,

$$P_{j+M}(u) = P_j(u)^n + \sum_{i=j}^{m-1} Q_i(u)^{n+1} + \sum_{i=m}^{j+M-1} Q_i(u)^n \tag{20}$$

Observe that the products $P_{j+M}(u)^2$ in (18) are evaluated in $\mathbf{V}_{j+M}$, as indicated by the use of the operator $\mathcal{R}_{j+M}[\cdot]$.

4.3.3. Resolved field

Once the detail coefficients are known at the required number of levels, the convective and viscous SGS terms (11) and (12) can be estimated by assuming

$$P_J(u) \approx P_{j+M}(u) = P_j(u)^n + \sum_{i=j}^{j+M-1} Q_i(u)^{n+1} \tag{21}$$

which leads to

$$\partial_j^{(1)}\mathcal{C}_j^{n+1} \approx \frac{1}{2}\left\{P_j\frac{\partial}{\partial x}\mathcal{R}_{j+M}[P_{j+M}(u)]^2 - P_j\frac{\partial}{\partial x}\mathcal{R}_j^{j+1}\left[P_j(u)^n\right]^2\right\} \tag{22}$$

$$\partial_j^{(11)}\mathcal{D}_j^{n+1} \approx \frac{1}{Re}\left\{P_j\frac{\partial^2}{\partial x^2}P_{j+M}(u) - P_j\frac{\partial^2}{\partial x^2}P_j(u)^n\right\} \tag{23}$$

Relations (22) and (23) can now be used in (10) to compute the resolved field at the new time step: $P_j(u)^{n+1}$. Note that the manner in which the solution has been time advanced does not fully correspond to the Euler method. This is merely a choice at this preliminary stage of the method implementation, and is not intended to suggest a specific way of proceeding to the solution.

Although it may appear that this approach is equivalent to solving on a fine mesh at level $j + M$, of size $\Delta_{j+M} = 2^{-(j+M)}$, this is not exactly the case. It should be noted that *only the projections of this fine-mesh solution and its derivatives onto the LES coarse grid are reliable*. This is fundamental if one aims to obtain a good quality coarse-grained solution. Accurately solving for $P_{j+M}(u)$ would require the computation of the wavelet coefficients at levels higher than $j + M - 1$.

4.4. Navier–Stokes equations in wavelet bases

This section deals with the extension of the methodology to the full 3D problem. The non-dimensional incompressible N–S equations read

$$\frac{\partial u_k}{\partial x_k} = 0 \tag{24}$$

$$\frac{\partial u}{\partial t} + \frac{\partial}{\partial x_k}(u_k u_l) = -\frac{\partial p}{\partial x_k} + \frac{1}{Re}\frac{\partial^2 u_k}{\partial x_l^2} \tag{25}$$

where Re is the Reynolds number based on characteristic scales of the problem. The projection of the system of Eqs. Eqs. (24) and (25) on the LES grid $\mathbf{V}_j^3$ yields

Continuity equation

$$P_j^3\frac{\partial}{\partial x_k}P_j^3(u_k) = -P_j^3\frac{\partial}{\partial x_k}\left(P_j^3(u_k) - P_j^3(u_k)\right) \tag{26}$$

Momentum equation

$$\frac{\partial}{\partial t}P_j^3(u_k) + P_j^3\frac{\partial}{\partial x_l}\left(P_j^3(u_k)P_j^3(u_l)\right) + P_j^3\frac{\partial}{\partial x_k}P_j^3(p) - \frac{1}{Re}P_j^3\frac{\partial^2}{\partial x_l^2}P_j^3(u_k) =$$

$$-P_j^3\frac{\partial}{\partial x_l}\left(P_j^3(u_k)P_j^3(u_l) - P_j^3(u_k)P_j^3(u_l)\right) \tag{27}$$

$$+\frac{1}{Re}P_j^3\frac{\partial^2}{\partial x_l^2}\left(P_j^3(u_k) - P_j^3(u_k)\right) \tag{28}$$

$$-P_j^3\frac{\partial}{\partial x_k}\left(P_j^3(p) - P_j^3(p)\right) \tag{29}$$

where the differences $\left\{P_j^3(f) - P_j^3(f)\right\}$ represent the unknown subgrid field $Q_{j,SGS}^3(f)$ given by

$$Q_{j,SGS}^3(f) = \sum_{i=j}^{J-1}\left(\sum_{r=1}^{7} Q_i^{(r)}(f)\right) \tag{30}$$

Observe that, by comparison with the Burgers equation, the approximation of the N–S equations on $\mathbf{V}_j^3$ generates two additional closure terms. One comes from the continuity equation, r.h.s. of (26). We will call this the *mass conservation SGS term*. The other one emerges from the projection of the pressure term in the momentum Eq. (29). This term will be named the *pressure SGS term*.

A consequence of the lack of commutation between the derivative and the projection operations is that the resolved velocity field is not solenoidal. Hence, mass conservation is not guaranteed locally. This has already been observed by Geurts et al. in their study on commutation errors in LES based on non-uniform filters [27]. In their paper, the authors suggest that the commutation error which appears in the continuity equation may be associated with local creation and destruction of resolved mass, due to the non-uniformity of the filter. In a similar line of thinking, the emergence of a mass residual term in the wavelet-based LES equations could be attributed to the creation and destruction of large and small-scale mass across resolutions. Its function seems to be that of enforcing the continuity constraint on the fine grid $\mathbf{V}_{j+M}$. Note however, that this term can be calculated explicitly once the solution of the small-scale equations is known. Therefore, there is no need to model or treat this contribution separately. Below is a summary of the four subgrid terms present in the LES equations. In what follows the superscript "3" is dropped for clarity of notation. Unless otherwise stated, the operator $P_j(\cdot)$ is equivalent to $P_j^3(\cdot)$ in the 3D context.

Convective SGS term

$$\partial_j^{(l)}\mathcal{C}_{j,kl} = P_j\frac{\partial}{\partial x_l}(P_j(u_k)P_j(u_l) - P_j(u_k)P_j(u_l)) \tag{31}$$

$$= P_j\frac{\partial}{\partial x_l}(P_j(u_k)Q_{j,SGS}(u_l) + P_j(u_l)Q_{j,SGS}(u_k)) \tag{32}$$

$$+ P_j\frac{\partial}{\partial x_l}(Q_{j,SGS}(u_k)Q_{j,SGS}(u_l)) \tag{33}$$

Viscous SGS term

$$\partial_j^{(ll)}\mathcal{D}_{j,k} = \frac{1}{Re}P_j\frac{\partial^2}{\partial x_l^2}(P_J(u_k) - P_j(u_k)) = \frac{1}{Re}P_j\frac{\partial^2}{\partial x_l^2}Q_{j,SGS}(u_k) \tag{34}$$

Pressure SGS term

$$\partial_j^{(k)}\mathcal{P}_j = P_j\frac{\partial}{\partial x_k}(P_J(p) - P_j(p)) = P_j\frac{\partial}{\partial x_k}Q_{j,SGS}(p) \tag{35}$$

Mass conservation SGS term

$$\partial_j^{(k)}\mathcal{M}_{j,k} = P_j\frac{\partial}{\partial x_k}(P_J(u_k) - P_j(u_k)) = P_j\frac{\partial}{\partial x_k}Q_{j,SGS}(u_k) \tag{36}$$

4.5. 3D modelling approach

In a similar way as in 1D, we define a hierarchy of wavelet spaces $\mathbf{W}_m^{(r)}$, of sizes $\Delta_m = 2^{-3m}$. At each level m, there exist seven distinct wavelet subspaces, whose associated coefficients are defined by the projection of the momentum equations on $\mathbf{W}_m^{(r)},\ r = 1,\ldots,7$. In the M-level approach, this leads to a system of $r \times M$ equations for each of the three velocity components, namely,

$$\frac{\partial}{\partial t}Q_m^{(r)}(u_k) = -Q_m^{(r)}\frac{\partial}{\partial x_l}(u_k u_l) - Q_m^{(r)}\frac{\partial}{\partial x_k}(p) + \frac{1}{Re}Q_m^{(r)}\frac{\partial^2}{\partial x_l^2}(u_k) \tag{37}$$

where m ranges from j to $j + M - 1$. Based on the arguments developed in Section 4.2, the above equation may be simplified by truncating the MRA of the velocity field at level $j + M - 1$, which provides an approximation of the velocity in $\mathbf{V}_{j+M}$,

$$u_k \approx P_j(u_k) + \sum_{i=j}^{j+M-1}\left(\sum_{r=1}^{7}Q_i^{(r)}(u_k)\right) = P_{j+M}(u_k) \tag{38}$$

Substituting (38) into (37) provides

$$\frac{\partial}{\partial t}Q_m^{(r)}(u_k) = -Q_m^{(r)}\frac{\partial}{\partial x_l}(P_{j+M}(u_k)P_{j+M}(u_l)) + \frac{1}{Re}Q_m^{(r)}\frac{\partial^2}{\partial x_l^2}P_{j+M}(u_k) - Q_m^{(r)}\frac{\partial p}{\partial x_k} \tag{39}$$

Note that the pressure term $Q_m^{(r)}\partial_{x_k}p$ on the r.h.s of (39) is not known. Based on physical considerations, one can assume that this term is not linked to the generation or dissipation of energy in the domain. In fact, for incompressible flows, its role is to enforce continuity. It is therefore reasonable to assume that the action of $Q_m^{(r)}\partial_{x_k}p$ on the evolution of the small scales is unimportant, and its contribution can be ignored in (39).

4.6. Practical implementation in 3D

This section provides a set of guidelines for the practical implementation of our wavelet-based LES approach in 3D. The actual implementation has not been carried out and is left for future work.

4.6.1. Resolved non-linear term

The non-linear interactions between low-wavenumber modes lead to a transfer of energy down the turbulent cascade. Mathematically, this is reflected in the population of wavelet spaces at higher resolution levels. As discussed in Section 4.3, most of these newly generated structures reside at scales in the vicinity of $\mathbf{V}_j$. Hence, a reasonable approximation of the resolved advective term is

$$P_j\frac{\partial}{\partial x_l}P_j(u_k)P_j(u_l) \approx P_j\frac{\partial}{\partial x_l}\mathcal{R}_j^{j+1}[P_j(u_k)]\mathcal{R}_j^{j+1}[P_j(u_l)] \tag{40}$$

As in 1D, this is equivalent to reconstructing the resolved velocity field $P_j(u_k)$ in $\mathbf{V}_{j+1}^3$. In the finer space $\mathbf{V}_{j+1}^3$, one can then carry out ordinary multiplication of the coefficients, and apply the differential operator $\partial_j^{(l)}$, on $\mathbf{V}_j^3$, to the resulting field.

4.6.2. Closure terms

The evaluation of the wavelet coefficients in 3D is conceptually analogous to that in the Burgers problem. The main difference is the fact that the number of wavelet spaces has now increased sevenfold. At a generic level m the wavelet coefficients for each of the wavelet components, $r = 1,\ldots,7$, are calculated by

$$Q_m^{(r)}(u_k)^{n+1} = Q_m^{(r)}(u_k)^n + \Delta t\left\{-Q_m^{(r)}\frac{\partial}{\partial x_l}\mathcal{R}_{j+M}[P_{j+M}(u_k)]\mathcal{R}_{j+M}[P_{j+M}(u_l)] + Q_m^{(r)}\frac{1}{Re}\frac{\partial^2}{\partial x_l^2}P_{j+M}(u_k)\right\} \tag{41}$$

Note that the non-linear terms are evaluated in $\mathbf{V}^3_{j+M}$. The fine-grid approximation $P_{j+M}(u_k)$ is given in terms of the most recent available information at the time,

$$P_{j+M}(u_k) = P_j(u_k)^n + \sum_{i=j}^{m-1}\sum_{r=1}^{7} Q_i^{(r)}(u_k)^{n+1} + \sum_{i=m}^{j+M-1}\sum_{r=1}^{7} Q_i^{(r)}(u_k)^n \tag{42}$$

4.6.3. Resolved field

Having computed the required number of wavelet spaces, the SGS terms (31), (34) and (36), at time t_{n+1}, can be written as

$$\partial_j^{(l)} \mathcal{C}_{j,kl}^{n+1} \approx P_j \frac{\partial}{\partial x_l} \mathcal{R}_{j+M}[P_{j+M}(u_k)]\mathcal{R}_{j+M}[P_{j+M}(u_l)] - P_j \frac{\partial}{\partial x_l} \mathcal{R}_j^{j+1}\left[P_j(u_k)^n\right]\mathcal{R}_j^{j+1}\left[P_j(u_l)^n\right] \tag{43}$$

$$\partial_j^{(ll)} \mathcal{D}_{j,k}^{n+1} \approx \frac{1}{Re}\left\{ P_j \frac{\partial^2}{\partial x_l^2} P_{j+M}(u_k) - P_j \frac{\partial^2}{\partial x_l^2} P_j(u_k)^n \right\} \tag{44}$$

$$\partial_j^{(k)} \mathcal{M}_{j,k}^{n+1} \approx P_j \frac{\partial}{\partial x_k} P_{j+M}(u_k) - P_j \frac{\partial}{\partial x_k} P_j(u_k)^n \tag{45}$$

where $P_{j+M}(u_k)$ is given by

$$P_{j+M}(u_k) = P_j(u_k)^n + \sum_{i=j}^{j+M-1}\sum_{r=1}^{7} Q_i^{(r)}(u_k)^{n+1} \tag{46}$$

Using this new information, the coarse-grained velocity can be estimated from

$$P_j^\star(u_k) = P_j(u_k)^n + \Delta t\left\{ -\partial_j^{(l)}\left(\mathcal{R}_j^{j+1}\left[P_j(u_k)^n\right]\mathcal{R}_j^{j+1}\left[P_j(u_l)^n\right] - \mathcal{C}_{j,kl}^{n+1}\right) + \frac{1}{Re}\partial_j^{(ll)}\left(P_j(u_k)^n - \mathcal{D}_{j,k}^{n+1}\right)\right\} \tag{47}$$

Note that the pressure term has not been included in (47), and $P_j^\star(u_k)$ does not necessarily satisfy the continuity equation,

$$\partial_j^{(k)} P_j^\star(u_k) \neq -\partial_j^{(k)} \mathcal{M}_{j,k}^{n+1} \tag{48}$$

Thus, the velocity field has to be adjusted so that mass conservation is fulfilled, i.e. (48) becomes an identity. This is done through the pressure term in the way explained in the next section.

4.7. The pressure equation

The N–S equations do not provide an independent equation for the pressure. For incompressible flows, it is commonplace to interpret the pressure gradient as a parameter that serves to enforce the continuity constraint (24). A pressure-correction method may be employed to this end.

The velocity field at time $n+1$ can be determined from $P_j^\star(u_k)$ by adding a correction term, namely,

$$P_j(u_k)^{n+1} = P_j^\star(u_k) - \Delta t\left\{ P_j \frac{\partial}{\partial x_k} p \right\}^{n+1} \tag{49}$$

Taking the divergence of (49), and re-projecting the result on $\mathbf{V}_j$, yields

$$P_j \frac{\partial}{\partial x_k} P_j(u_k)^{n+1} - P_j \frac{\partial}{\partial x_k} P_j^\star(u_k) = -\Delta t P_j \frac{\partial}{\partial x_k}\left\{ P_j \frac{\partial}{\partial x_k} p \right\}^{n+1} \tag{50}$$

And since the velocity field at time t_{n+1} must satisfy (26), we can write

$$\Delta t P_j \frac{\partial}{\partial x_k}\left\{ P_j \frac{\partial}{\partial x_k} p \right\}^{n+1} = P_j \frac{\partial}{\partial x_k} P_j^\star(u_k) + \partial_j^{(k)} \mathcal{M}_{j,k}^{n+1} \tag{51}$$

which provides a Poisson-like equation for the pressure. The final velocity field is then obtained by substituting the solution of (51) into (49).

The approach presented here is not unique and other pressure-correction methods may be used for the evaluation of p. The purpose of this section is simply to show that our LES framework remains compatible with traditional numerical approaches.

In fact, the simplest approach would be to ignore the truncation errors in the continuity equation, i.e. $\partial_j^{(k)} \mathcal{M}_{j,k} = 0$, and use

$$P_j \frac{\partial}{\partial x_k} P_j(u) = 0 \tag{52}$$

The pressure term that appears in the large-scale momentum equations will thus be adjusted such that (52) is fulfilled locally on the LES grid $\mathbf{V}_j$. By contrast, the action of pressure on the small scales is ignored. Hence, the continuity constraint is not satisfied on the fine grids.

Another alternative is to use divergence-free basis functions, in which case (52) is automatically satisfied. However, for practical industrial problems where non-periodic boundary conditions or complex geometries have to be considered, the use of such wavelets might prove somewhat restrictive.

Finally, another option would be to use additional divergence-free projection, which can be achieved as usual by solving a Poisson equation.

4.8. Adaptivity: thresholding strategy

The final implementation of the LES technique should also incorporate an adaptive strategy able to exploit the sparseness property of the wavelet representation. To this end, we could use a simple thresholding technique in which the value of the threshold ϵ is defined by the user during the initialisation step. This strategy is similar to that used by Bacry et al. [11].

At the end of each time step, the wavelet spaces considered in the simulation $\mathbf{W}_m$, $m = j, \ldots, j + M - 1$, are inspected and those grid points associated with coefficients of absolute value smaller than ϵ are deactivated. If a particular node is associated with a large wavelet coefficient, then *halo* nodes are activated adjacent to it. Note that these re-activated grid points are adjacent to the significant coefficient not only in position, but also in scale. The ensemble of active nodes will therefore define the computational grid at the next time step. This algorithm is based on the hypothesis that during a time step, the solution does not move in space nor scale beyond the limits of the halo nodes.

4.9. Parallel implementation issues

It is clear that for practical three-dimensional LES it is necessary that the method should be able to run in parallel. This would be achieved using a classical domain-decomposition strategy in which blocks of geometrically-contiguous points are assigned to each processor in a parallel computer. Communication between adjacent blocks then requires an overlap region or *halo* surrounding each block. Such a strategy is facilitated in the present formulation by the compact support of the wavelets, which means that the width of the halo is limited to a fairly small number of points. For example, using Daubechies 6 wavelets the halo width is three points. Management of the adaptive property will already require the use of an octree type of data structure, which can be exploited also to facilitate both the domain decomposition and the necessary load-balancing. These are implementation issues not fundamental to the developed approach and will be addressed in future work.

5. A priori tests: Kolmogorov turbulence

In our wavelet-based LES framework, a so-called projected DNS quantity is obtained by operating on the full resolution field, defined in $\mathbf{V}_J$, then projecting the outcome on the coarse grid $\mathbf{V}_j$. The product of two variables is always performed in $\mathbf{V}_J$. On the other hand, an LES quantity is derived from the DNS field, by truncating its MRA decomposition at the prescribed level. The result of operating on this truncated field is then projected onto the coarse mesh $\mathbf{V}_j$. Multiplication of any two variables is carried out as explained in Section 4.3, for 1D, and Section 4.6 for the 3D problem. Unless otherwise stated, the LES grid belongs to level $j = 5$, i.e. the coarse-grained field is defined by 32 points in each of the axis directions.

5.1. A priori tests: turbulent time series (TTS)

The convective and viscous closure terms, (11) and (12), respectively, have been analysed for an atmospheric turbulent time series, called here TTS. The source of these data can be found in [28], where a detailed description of the experimental parameters is provided. Only the horizontal component of the velocity field is considered here, from which the mean has been removed. Making use of Taylor's hypothesis, the data is split into 32 series of 2^{10} samples. The averaged spectrum is shown in Fig. 1(a), which highlights the existence of an inertial subrange over a few octaves.

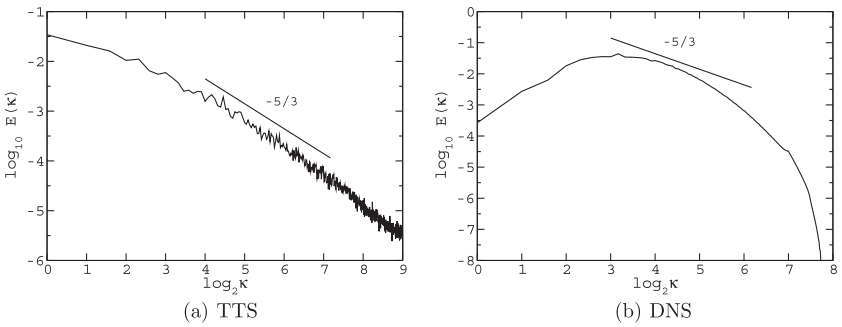

Fig. 1. Fourier spectra $E(\kappa)$ of data sets.

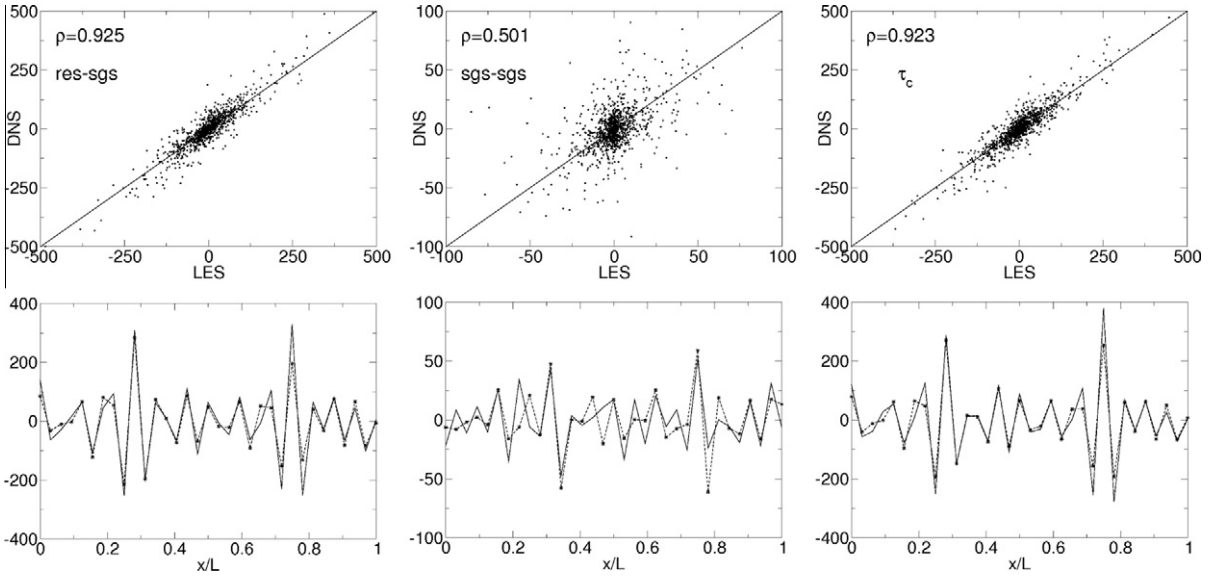

Fig. 2. [TTS] Convective SGS term ($j = 5$, $M = 1$). From left to right: RES–SGS interactions: $\partial_j^{(1)}(u_i u_j')$; SGS–SGS interactions: $\partial_j^{(1)} u_j'^2$; Total SGS term: $\partial_j^{(1)} C_j$. The upper panels show the correlations between exact and approximation values. The lower panels compare typical 1D realizations of these fields (– DNS; –∗– LES).

5.1.1. Convective closure term

To assess the accuracy of the methodology in capturing the main features of the convective subgrid field, the latter has been decomposed into its RES–SGS and SGS–SGS components, as defined in Section 4.1. This is illustrated in Fig. 2, for a one-level approach ($M = 1$), and in Fig. 3, for a two-level approach ($M = 2$). These results reveal the high fidelity with which the method represents the correlations between resolved and subgrid scales, as shown by the high values of the correlation coefficient, ρ, above 0.9. The structure and order of magnitude of the SGS–SGS interaction term is relatively well captured, although there is a clear loss of accuracy with respect to the RES–SGS component. Not surprisingly, the two-level approach leads to a substantial improvement in the SGS–SGS correlation, which is a direct consequence of the closure problem of turbulence. However, the fact of adding a second level does not appear to have a significant effect on the RES–SGS term. This is in agreement with previous findings [29,30], and illustrates the fact that the transfer of energy between resolved and subgrid

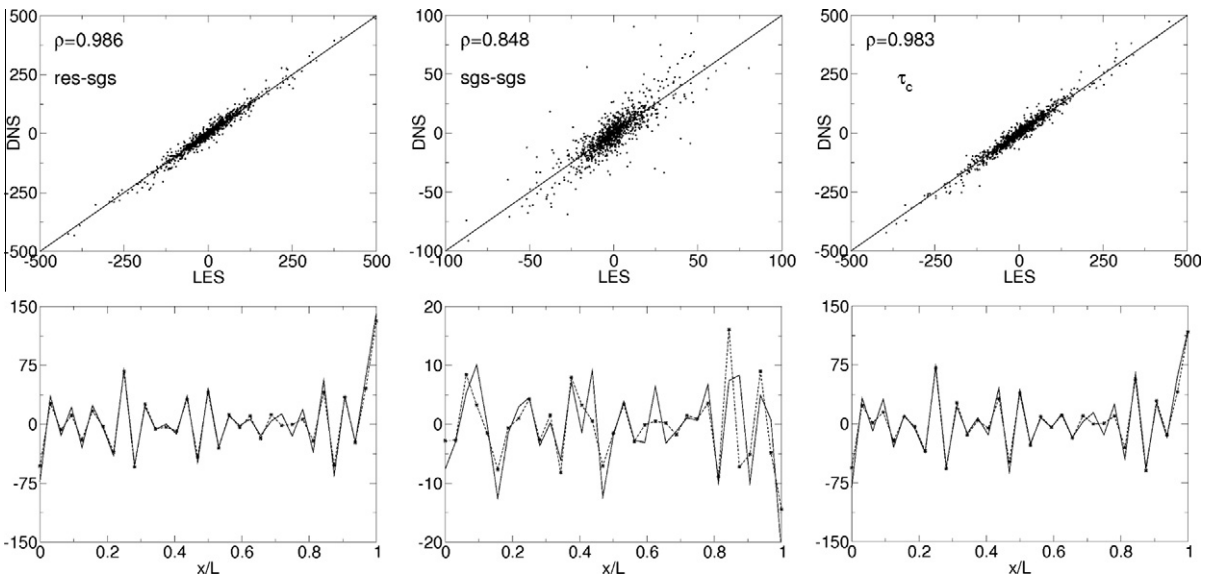

Fig. 3. [TTS] Convective SGS term ($j = 5$, $M = 2$). From left to right: RES–SGS interactions: $\partial_j^{(1)}(u_i u_j')$; SGS–SGS interactions: $\partial_j^{(1)} u_j'^2$; Total SGS term: $\partial_j^{(1)} C_j$. The upper panels show the correlations between exact and approximation values. The lower panels compare typical 1D realizations of these fields (– DNS; –∗– LES).

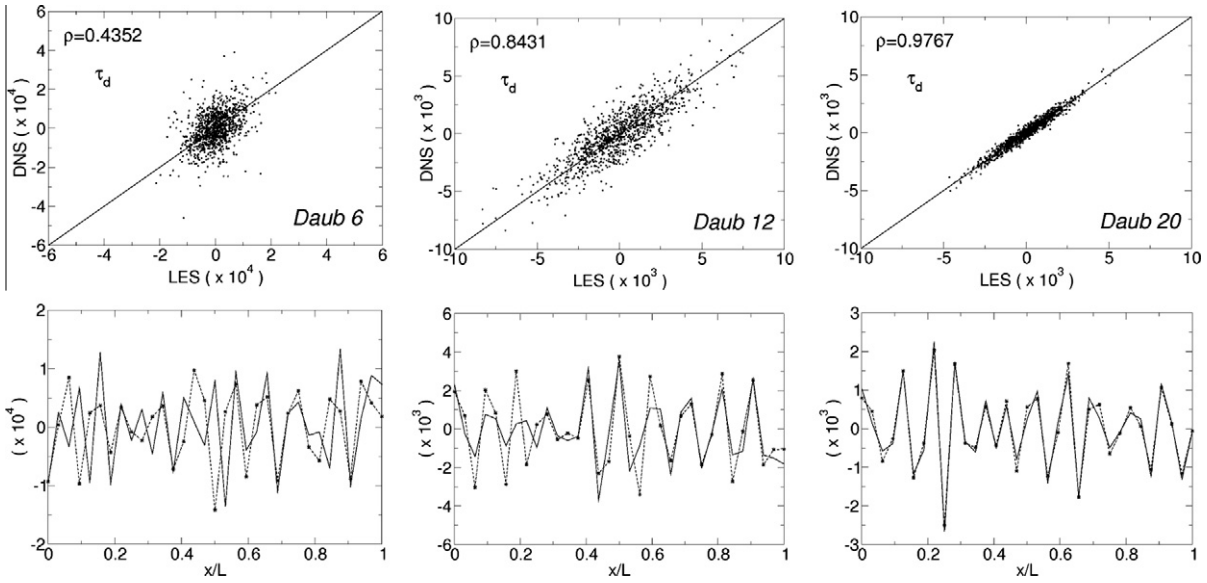

Fig. 4. [TTS] Viscous SGS term ($j = 5,\ M = 1$) : $\partial_j^{(11)} u'_j$. From left to right: *Daub 6*; *Daub 12*; *Daub 20*. The upper panels show the correlations between exact and approximation values. The lower panels compare typical 1D realizations of these fields (– DNS; –∗– LES).

modes is mainly due to interactions between adjacent scales. These graphs also show that the contribution of the RES–SGS correlations to the total SGS term $\partial_j^{(1)} \mathcal{C}_j$ prevails over that of the SGS–SGS component.

5.1.2. Viscous closure term

The exact viscous SGS term, defined by (12), and its LES approximation, given by (23), are compared in Fig. 4 for $M = 1$. Note that the values displayed on these graphs correspond to $\partial_j^{(11)} \mathcal{D}_j / \nu$. Fig. 4 shows the result of using wavelet bases with increasing number of vanishing moments. The number of vanishing moments is related to the degree of regularity of the wavelet function, and therefore to the rate of convergence of the wavelet series and that of its derivatives. This is made clear in Fig. 4, where a dramatic increase of the correlation coefficient is observed when the *Daub 12* (six vanishing moments) and *Daub 20* (ten vanishing moments) filters are employed.

From *a posteriori* tests on the Burgers equation, we believe that, for very high-Reynolds-number flows, the action of $\partial_j^{(11)} \mathcal{D}_j$ in the evolution Eq. (10) can be safely neglected. Evidence of this is given in Section 6. An *a priori* estimate of the relative importance of the viscous SGS term with respect to the convective SGS term can be obtained by taking the ratio of the characteristic values of each of these fields. The results displayed in Figs. 2 and 4 can be used to obtain an order of magnitude of $\partial_j^{(1)} \mathcal{C}_j$ (~ 100) and $\partial_j^{(11)} u'_j$ ($\sim 10^4$), respectively. The kinematic viscosity ν can be roughly evaluated by considering the average temperature of the air during the experiment, approximately 32 °C, which leads to a value of $\nu \approx 1.6 \times 10^{-5}$ m^2/s. We also need to take into account the duration of the experiment which has not been considered in the study of the correlations shown above. According to the source of the data, the acquisition time was 9.75 min. A conservative estimate is thus given by

$$\frac{\text{Diffusion}}{\text{Convection}} = \frac{\nu \partial_j^{(11)} u'_j}{\partial_j^{(1)} \mathcal{C}_j} \sim \frac{1.6 \times 10^{-5} \times 10^4}{100 \times (9.75/32) \times 60} = 8.75 \times 10^{-5} \ll 1 \tag{53}$$

which shows that the contribution of subgrid diffusion to the evolution of the large scales is likely to be insignificant relative to that of subgrid convection.

5.2. A priori tests: DNS turbulence (DNS)

The reliability of the proposed technique as a means of solving the coarse-grained N–S equations is judged through *a priori* tests on a DNS of decaying homogeneous isotropic turbulence. The flow field was computed using a pseudo-spectral code [31]. The solution domain is defined by 256^3 points, for a computational Reynolds number of 5000. The simulation was run for about 1.5 eddy-turnover times in order to obtain a well developed spectrum (see Fig. 1(b)). Unless otherwise stated, a one-level approach is always considered in these analyses.

5.2.1. Convective closure term

Figs. 5 and 6 compare the projected DNS and the LES approximation of the RES–SGS and the SGS–SGS components of the convective SGS term. The sum of these two terms, encompassed in $\partial_j^{(l)} \mathcal{C}_{j,kl}$, is shown in Fig. 7. Only the contributions involved

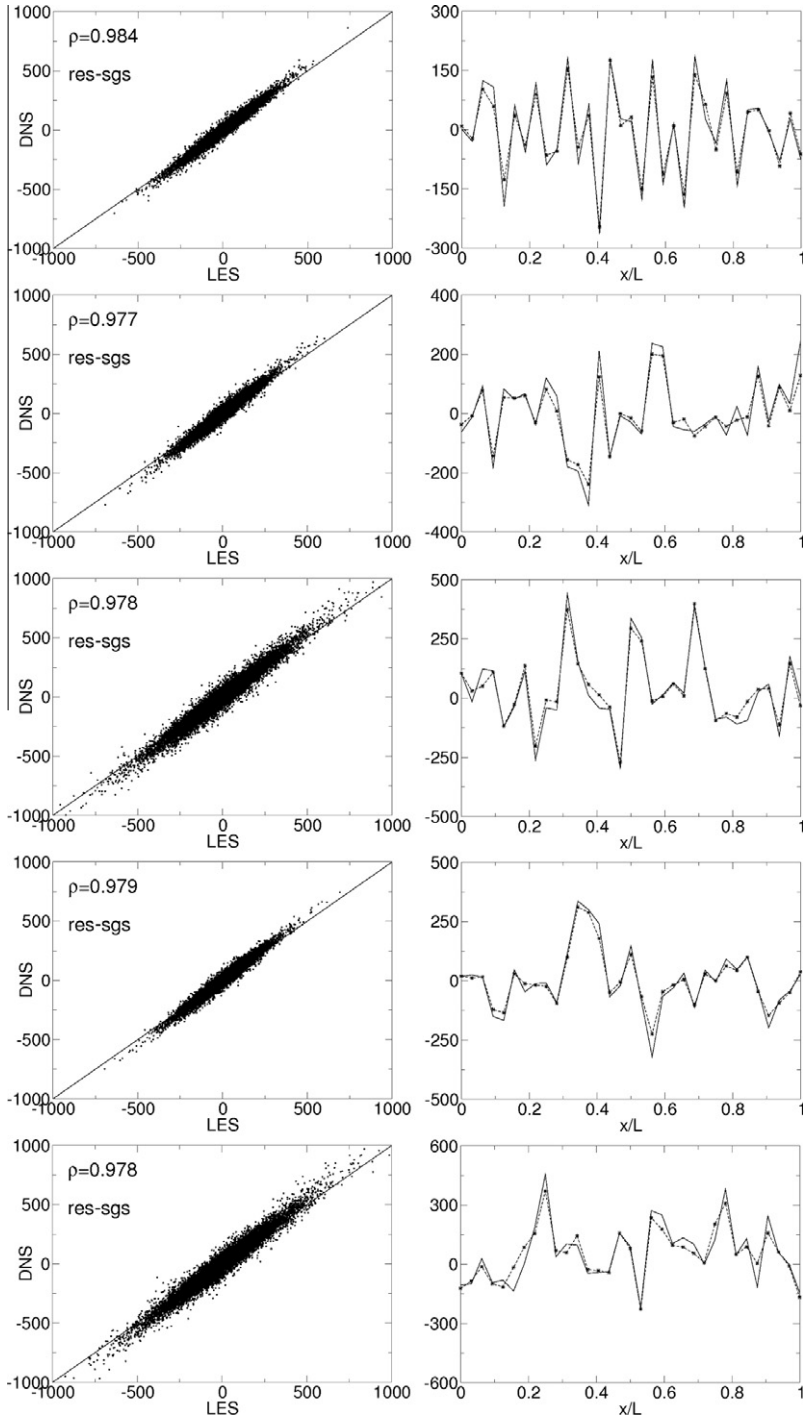

Fig. 5. [DNS] RES–SGS interaction terms in the x-momentum equation ($j = 5$, $M = 1$). From top to bottom: $\partial_j^{(1)} u_j u_j'$, $\partial_j^{(2)} u_j v_j'$, $\partial_j^{(2)} u_j' v_j$, $\partial_j^{(3)} u_j w_j'$, $\partial_j^{(3)} u_j' w_j$. The left-hand side panels show the correlations between exact and approximation values. The right-hand side panels compare typical 1D intersections of these fields (– DNS; –∗– LES).

in the x-momentum equation are presented here. The study of the six other components yielded similar results, as anticipated for an isotropic flow.

The correlation coefficients for the RES–SGS component take on values very close to unity, being around 10% lower for the SGS–SGS component. This is in agreement with the conclusions drawn from the study of the atmospheric data. The better approximation obtained here is partly due to the fact that in the DNS data the power spectrum of the turbulence exhibits

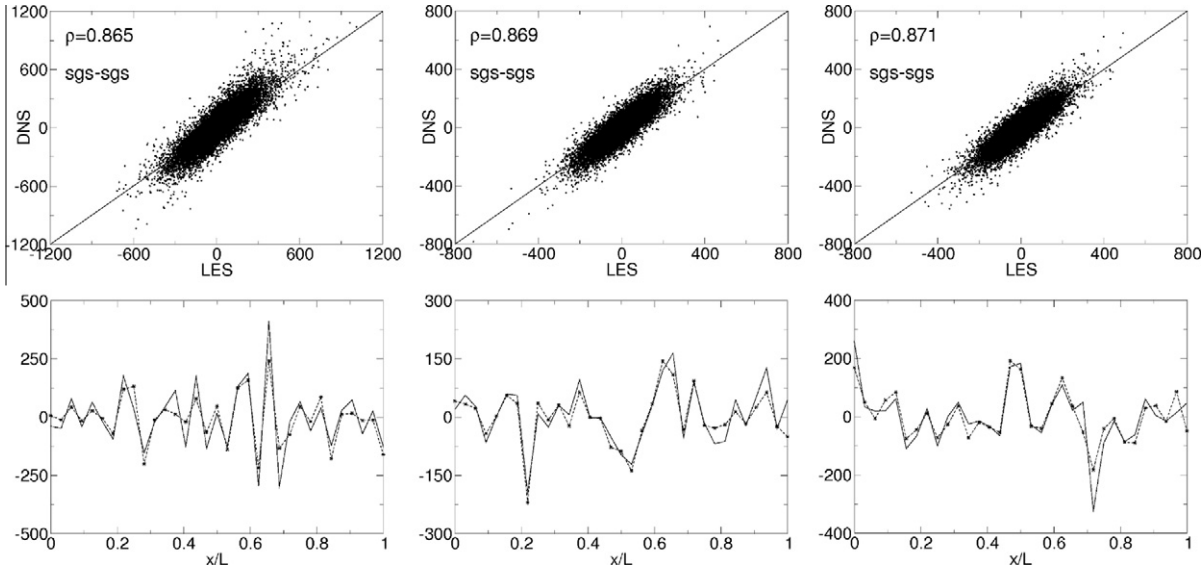

Fig. 6. [DNS] SGS–SGS interaction terms in the x-momentum equation ($j = 5$, $M = 1$). From left to right: $\partial_j^{(1)} u_j'^2$, $\partial_j^{(2)} u_j' v_j'$, $\partial_j^{(3)} u_j' w_j'$. The upper panels show the correlations between projected DNS and LES model values. The lower panels compare typical 1D intersections of these fields (– DNS; −*− LES).

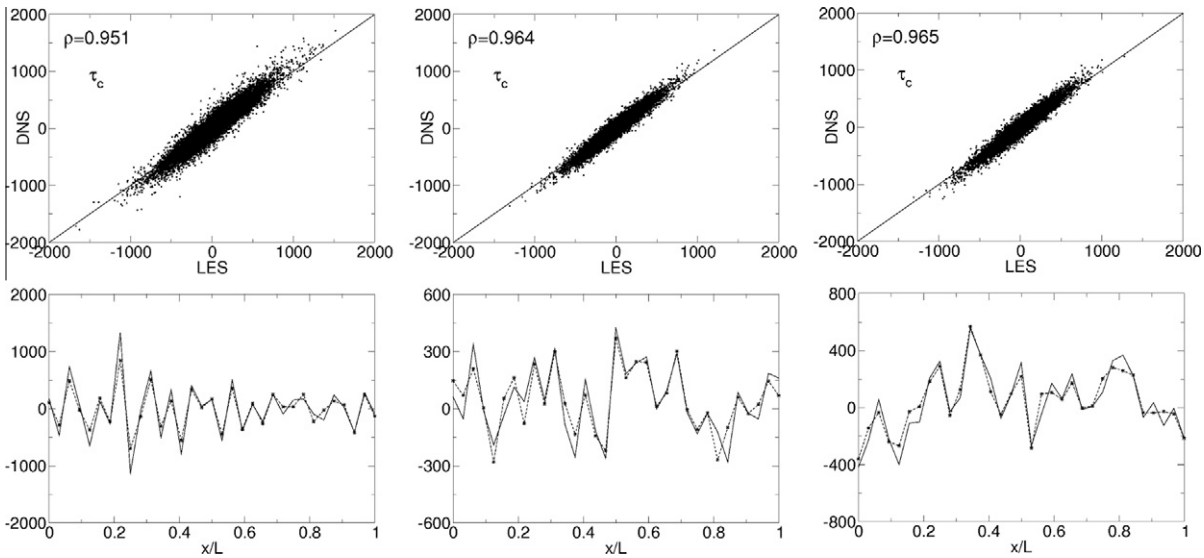

Fig. 7. [DNS] Total convective SGS terms in the x-momentum equation ($j = 5$, $M = 1$). From left to right: $\partial_j^{(1)} C_{j.11}$, $\partial_j^{(2)} C_{j.12}$, $\partial_j^{(3)} C_{j.13}$. The upper panels show the correlations between projected DNS and LES model values. The lower panels compare typical 1D intersections of these fields (– DNS; −*− LES).

a slightly steeper slope at the LES cut-off wavenumber (Reynolds number is lower). The correlation coefficients for all nine components of $\partial_j^{(l)} C_{j,kl}$ in the momentum equation turned out to be in the order of 0.95, as expected, a little lower than those found for the RES–SGS terms.

5.2.2. Viscous closure term

The results of the study of the diffusion SGS terms (34), in the x-momentum equation, are displayed in Fig. 8 in which the *Daub 6* wavelets have been employed. To see the effect of the wavelet basis on the correlation coefficient, Fig. 9 shows the component $\partial_j^{(11)} u_j'$ based on Daubechies wavelets with different numbers of vanishing moments. Note that the values shown on these graphs correspond to $Re\partial_j^{(ll)} \mathcal{D}_{j,k}$. A careful examination of these graphs leads to the same conclusions reached in the previous section. The poorer correlations obtained when the *Daub 6* filter is used are traced to the lower order of the corresponding derivative operator and low-pass filter (wavelet projection) which are effectively related to the regularity of the wavelets (see Chapter 6 in [32] for a detailed analysis of the performance of differential operators in various wavelet basis).

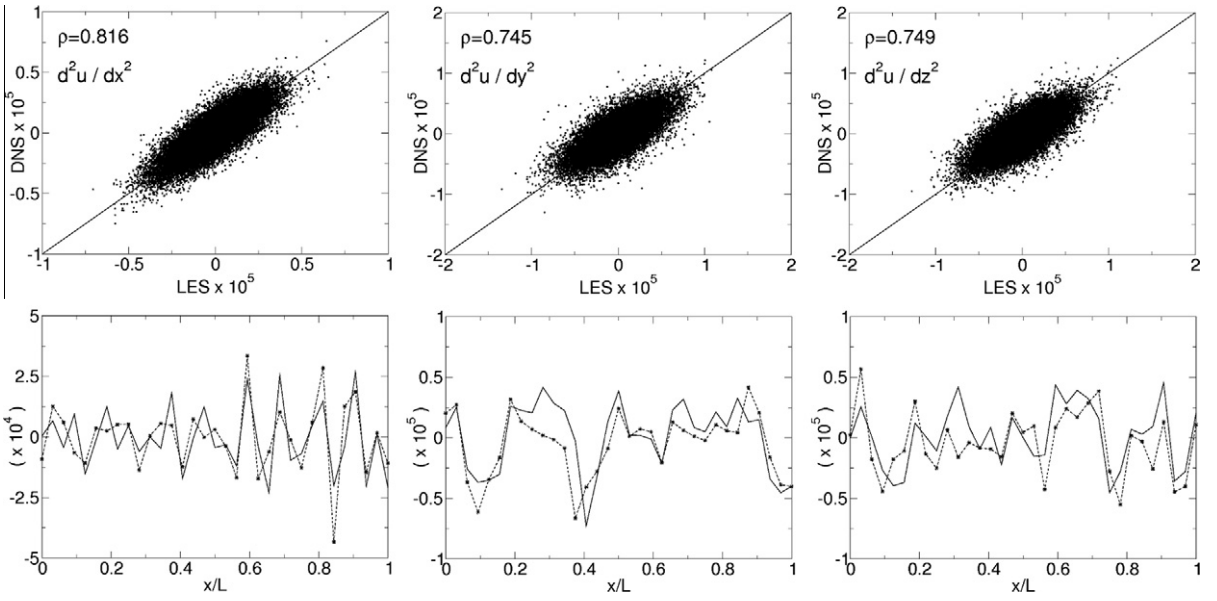

Fig. 8. [DNS] Diffusion SGS terms in the x-momentum equation ($j = 5$, $M = 1$). Wavelets basis: *Daub 6*. From left to right: $\partial_j^{(11)} u_j'$, $\partial_j^{(22)} u_j'$, $\partial_j^{(33)} u_j'$. The upper panels show the correlations between projected DNS and LES model values. The lower panels compare typical 1D intersections of these fields (– DNS; –∗– LES).

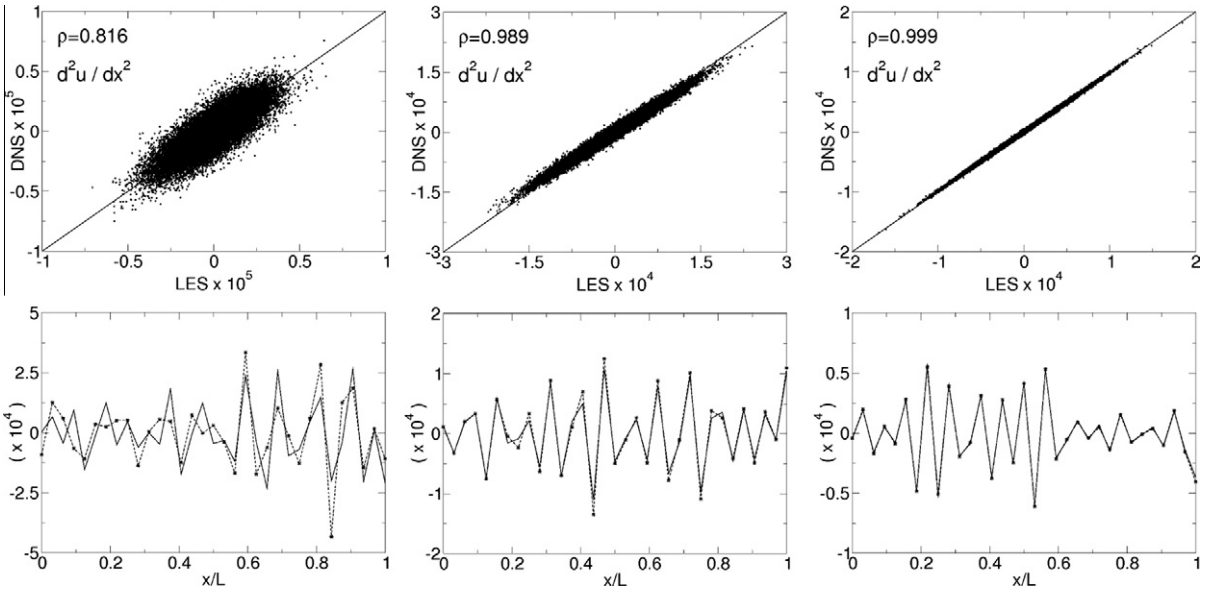

Fig. 9. [DNS] Diffusion SGS terms in the x-momentum equation ($j = 5$, $M = 1$). From left to right: Viscous component $\partial_j^{(11)} u_j'$ in wavelet bases *Daub 6*, *Daub 12* and *Daub 20*. The upper panels show the correlations between projected DNS and LES model values. The lower panels compare typical 1D intersections of these fields (– DNS; –∗– LES).

Employing wavelets with more vanishing moments speeds up the convergence of the series, and leads to much better correlations between exact and model values, as seen from the plots shown in Fig. 9. As was done for the atmospheric data, one can study the significance of the diffusion SGS term with respect to the total convective SGS term. The characteristic values of these fields can be obtained by inspection of the graphs in Figs. 7 and 8, which provides $\partial_j^{(1)} \mathcal{C}_{j,11} \sim 10^3$ and $\partial_j^{(11)} u_j' \sim 5 \times 10^4$. The kinematic viscosity (non-dimensional) in the DNS computation was $\nu = 2 \times 10^{-4}$. This leads to the following estimate:

$$\frac{\text{Diffusion}}{\text{Convection}} = \frac{\partial_j^{(11)} u_j'}{Re\,\partial_j^{(1)} \mathcal{C}_{j,11}} \sim \frac{2 \times 10^{-4} \times 5 \times 10^5}{10^3} = 0.01 \ll 1 \tag{54}$$

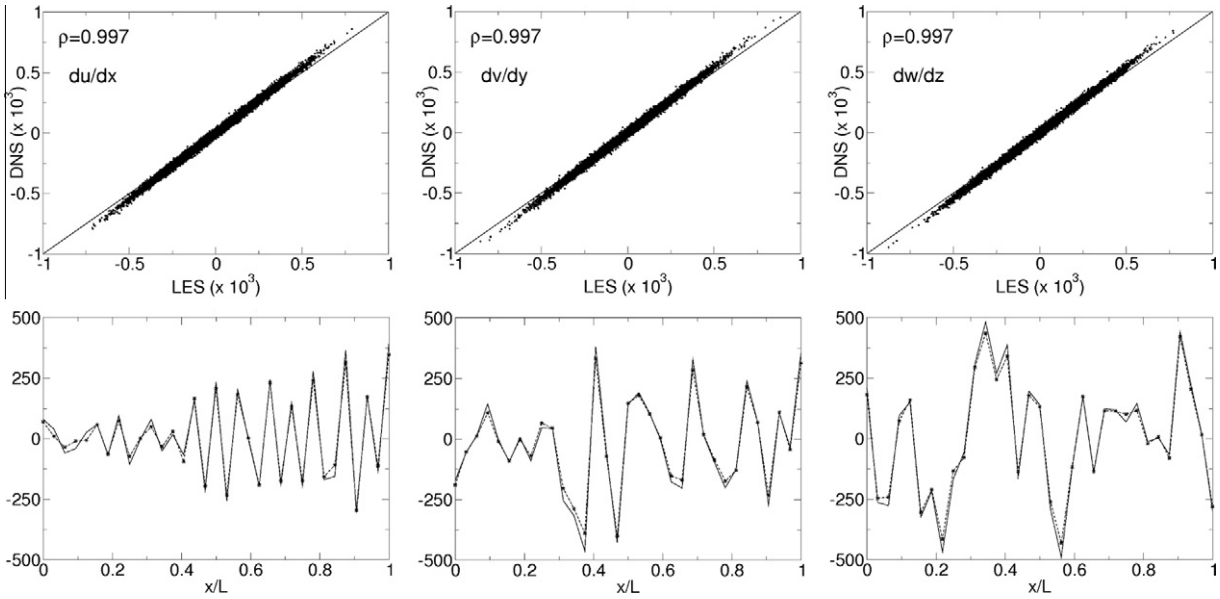

Fig. 10. [DNS] Mass conservation SGS term ($j = 5$, $M = 1$). From left to right: $\partial_j^{(1)} u_j'$, $\partial_j^{(2)} v_j'$, $\partial_j^{(3)} w_j'$. The upper panels show the correlations between projected DNS and LES model values. The lower panels compare typical 1D intersections of these fields (– DNS; –∗– LES).

Table 1
Parameters of the Burgers simulations.

Simulation	*Re*	*J*	*j*	*M*
DNS-Lo	2000	12	–	–
LES-Lo1	2000	12	7	1
LES-Lo2	2000	12	7	2
DNS-Hi	15,000	15	–	–
LES-Hi2	15,000	15	7	2

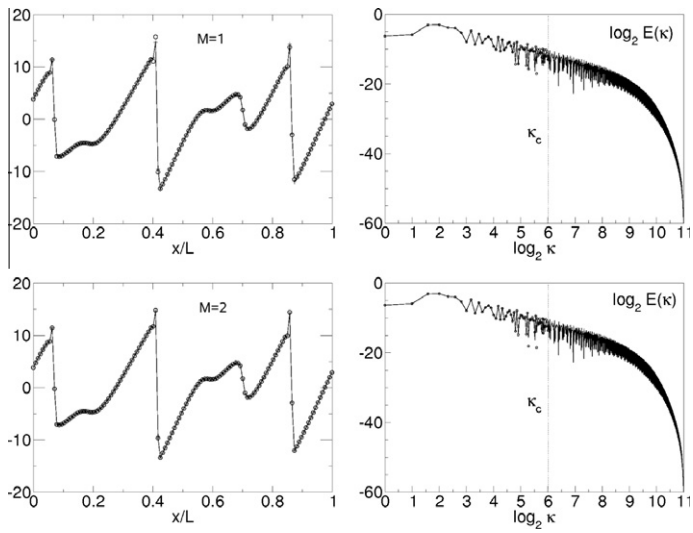

Fig. 11. [$Re = 2000$] Solution of the LES Burgers equation at time $t = 0.03$ s ($J = 12$, $j = 7$). Left: Velocity profiles (–+– DNS; ∘ LES). Right: Corresponding Fourier spectra (– DNS; ∘ LES). Upper panels: $M = 1$. Lower panels: $M = 2$.

which provides further support to the claim that subgrid convection prevails over subgrid diffusion in the large-scale equations.

5.2.3. Mass conservation closure term

The two additional SGS terms which appear in the 3D problem are the pressure and the mass conservation SGS terms. The evaluation of the pressure SGS term does not seem to be crucial to the solution of the large-scale equation. As explained in Section 4.7, this term can be added to the large-scale pressure component $\partial_j^{(k)} p_j$, and therefore does not need to be modelled explicitly. The mass conservation SGS term is analysed in Fig. 10. If we compare these results with those shown in Fig. 7 for the convective SGS term, we observe that the agreement between the projected DNS and the LES values is now considerably better. We can therefore conclude that, if the non-linear SGS terms are accurately predicted, it is very likely that this term will also be adequately reproduced.

6. A posteriori tests: Burgers turbulence

Burgers turbulence possesses two important features in common with real turbulence, namely, the existence of a non-linear spectral energy cascade, and the presence of small-scale regions dominated by the effects of viscosity. The formation of shocks is the most peculiar dynamic property of the Burgers equation. Two distinct characteristic length scales may be identified in Burgers turbulence: a large scale, associated with the energy-containing modes, and a small scale, of the order of the width of the shock fronts, linked to the dissipation process.

This section reports the main results of the application of our wavelet-based approach to the solution of the LES Burgers equation. For each LES simulation, the associated full resolution DNS field has also been computed for comparison. An initial Gaussian random field is prescribed by means of a Batchelor–Townsend spectrum [33]. No external forcing is applied, and the solution consists of a freely decaying ensemble of shock fronts. The large-scale solution at time zero is specified by projecting the corresponding initial DNS field on the coarse mesh, $\mathbf{V}_j$. A low and a very high value of the Reynolds number have been considered. The parameters of the simulations carried out are listed in Table 1.

6.1. Burgers LES: Re = 2000

Figs. 11 and 12 compare the outcome of the simulations *LES-Lo1* and *LES-Lo2*, with the coarse-grid projection of *DNS-Lo*. Observe that in both cases the velocity profiles are very well reproduced overall. As expected, the maximum relative errors occur in the vicinity of the shocks, with levels of about 7% at $x/L = 0.417$, when only one level is considered, and around 1% at $x/L = 0.874$, for two levels. The resolved part of the spectrum ($\kappa_c < 2^{j-1}$) is very well represented in both LES configurations, which capture with high fidelity the κ^{-2} power law, characteristic of fully developed Burgers turbulence. This is consistent with the excellent match found for the time evolution of the total kinetic energy and dissipation between the projected DNS and the LES solutions, as shown in Fig. 12. The dissipation field, defined here as

$$\frac{\varepsilon(t)}{15\nu} = \left\langle \left(P_j \frac{\partial}{\partial x} P_j(u) \right)^2 \right\rangle \tag{55}$$

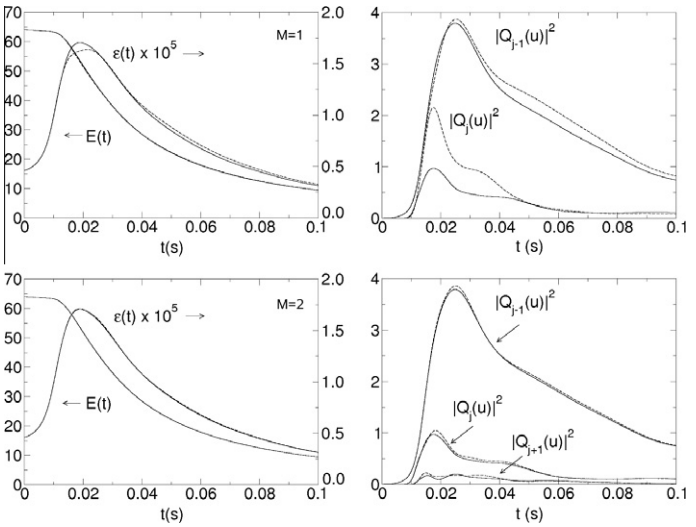

Fig. 12. [$Re = 2000$] Solution of the LES Burgers equation ($J = 12$, $j = 7$). Left: Total energy, $E(t)$, and dissipation, $\varepsilon(t)/15\nu$. Right: Variance of the wavelet coefficients at level $j-1$:$|Q_{j-1}(u)|^2$, level j: $|Q_j(u)|^2$, and level $j+1$:$|Q_{j+1}(u)|^2$. In all graphs: (– DNS; – – LES). Upper panels: $M = 1$. Lower panels: $M = 2$.

is very accurately reproduced by *LES-Lo2*. On the other hand, the solution of *LES-Lo1* exhibits a slightly lower level of dissipation near the peak zone ($t \approx 0.02$ s). Nevertheless, these discrepancies disappear as time evolves.

It is also interesting to study the evolution of the wavelet coefficient energy over time. The variance of the wavelet coefficients provides information relative to the energetic content of the small scales associated with a particular range of wavenumbers. The temporal variation of the wavelet energy has thus been investigated at the resolved level, given by $\langle d^2_{j-1,k}\rangle$, at the lowest small-scale level j, given by $\langle d^2_{j,k}\rangle$, and at the highest small-scale level considered in the simulation $j+1$, given by $\langle d^2_{j+1,k}\rangle$ (only for $M = 2$). In the graphs, $|Q_i(u)|^2$ refers to the energy of the wavelet coefficients at resolution i, defined as

$$|Q_i(u)|^2 = \langle d^2_{i,k}\rangle = \frac{1}{2^i}\sum_{k=1}^{2^i} d^2_{i,k} \tag{56}$$

where $d_{i,k}$ are the wavelet coefficients of the projection of u on $\mathbf{W}_i$. The lower right-hand plot in Fig. 12 shows the good agreement between DNS and LES for case *LES-Lo2*. A lower level of agreement is obtained when the second level is dropped (upper right-hand plot in Fig. 12). In this case, the energetics of the wavelet coefficients at the resolved level are relatively well captured, whereas those of the small-scale velocity field are overestimated. This can be attributed to aliasing effects, which arise from the truncation of the Burgers equation at subspace $\mathbf{W}_j$. In this case, the extra energy which could not be transferred down the cascade (to subspace $\mathbf{W}_{j+1}$), is being aliased back to the small-scale field, in $\mathbf{W}_j$. In fact, in a two-level approach, the additional subspace $\mathbf{W}_{j+1}$ may be regarded as a "bin" where the high-wavenumber modes generated by the non-linearities in the equation for $Q_j(u)$ can be realistically dissipated.

6.2. Burgers LES: Re = 15,000

Increasing the Reynolds number has the effect of steepening the gradients in the velocity field, and therefore reducing the size of the dissipative scales. At this Reynolds number and when the LES grid is defined by only 128 nodes, capturing the detailed structure of the resolved field near the shock fronts requires the use of a two-level approach.

Fig. 13 compares the velocity profile and associated Fourier spectrum, solution of *LES-Hi2*, with those obtained by projecting *DNS-Hi*. The agreement between the LES and DNS velocity fields is relatively good; despite the presence of severe gradients in the flow, which are very well represented by the coarse-mesh solution. Once more, the maximum relative errors are found in the neighbourhood of the shock fronts, being of the order of 13% at $x/L = 0.315$. Despite these local errors in the velocity field, the LES spectrum reproduces with great reliability the resolved part of the DNS energy spectrum. The temporal decay of the total energy and dissipation is compared with that of the projected DNS in Fig. 14. The evolution of the total energy is very well represented by the LES solution. The level of dissipation appears to be slightly lower than in the DNS, though the trend and the order of magnitude of the dissipation field are well captured. The time evolution of the wavelet energy is shown in Fig. 15, where we can appreciate the good agreement between the LES and the DNS solutions, except

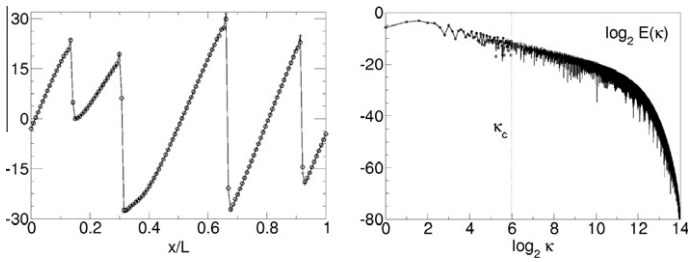

Fig. 13. [$Re = 15{,}000$] Solution of the LES Burgers equation at time $t = 0.06$ s ($J = 15$, $j = 7$, $M = 2$). Left: Velocity profile (– + – DNS; ∘ LES). Right: Corresponding Fourier spectrum (– DNS; ∘ LES).

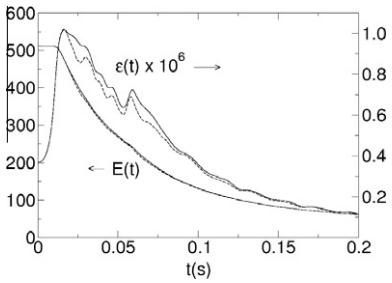

Fig. 14. [$Re = 15{,}000$] Time evolution of total energy, $E(t)$, and dissipation, $\varepsilon(t)/15\nu$, for the LES Burgers equation ($J = 15$, $j = 7$, $M = 2$), (– DNS; – – LES).

for the finest scale $j+1$. Observe the accumulation of energy that takes place at this level. The comments made earlier on the implications of considering a second level in the simulations hold equally here. The wavelet coefficients at level $j+1$ seem to act as a sink of energy which stabilises the solution, and their detailed dynamics do not seem to play a significant role on the development of the coarse-grained velocity.

6.3. Effect of the viscous subgrid terms

This section investigates the significance of the viscous terms present in the large and small-scale Burgers equations. The LES configurations *LES-Lo2* and *LES-Hi2*, studied in the previous section (see Table 1), have been considered for analysis. Recall that in the two-level approach the flow solution is governed by Eqs. (10) and (16), with $m = j$ and $j+1$. In order to bring out the contributions from the different scales represented in the simulation, the viscous terms are split apart in the following way:

$$\frac{\partial}{\partial t}P_j(u) + \frac{1}{2}P_j\frac{\partial}{\partial x}P_j(u)^2 - \overbrace{\frac{1}{Re}P_j\frac{\partial^2}{\partial x^2}P_j(u)}^{D_0^P} = -\frac{1}{2}P_j\frac{\partial}{\partial x}\left(P_{j+2}(u)^2 - P_j(u)^2\right) + \underbrace{\frac{1}{Re}P_j\frac{\partial^2}{\partial x^2}\left(Q_j(u)+Q_{j+1}(u)\right)}_{D_0^Q} \tag{57}$$

$$\frac{\partial}{\partial t}Q_j(u) + \frac{1}{2}Q_j\frac{\partial}{\partial x}P_{j+2}(u)^2 = \underbrace{\frac{1}{Re}Q_j\frac{\partial^2}{\partial x^2}P_j(u)}_{D_1^P} + \underbrace{\frac{1}{Re}Q_j\frac{\partial^2}{\partial x^2}(Q_j(u)+Q_{j+1}(u))}_{D_1^Q} \tag{58}$$

$$\frac{\partial}{\partial t}Q_{j+1}(u) + \frac{1}{2}Q_{j+1}\frac{\partial}{\partial x}P_{j+2}(u)^2 = \underbrace{\frac{1}{Re}Q_{j+1}\frac{\partial^2}{\partial x^2}P_{j+1}(u)}_{D_2^P} + \underbrace{\frac{1}{Re}Q_{j+1}\frac{\partial^2}{\partial x^2}Q_{j+1}(u)}_{D_2^Q} \tag{59}$$

where at each particular level the contributions from scales larger than those represented at that level, are tagged as D_n^P, and those from scales of the size of the represented scales, or smaller, are denoted by D_n^Q. Note that in (57) the definition of these terms is slightly different, as in fact, D_0^P only contains information from the resolved scales $P_j(u)$, whereas D_0^Q represents the contributions from all small scales in the simulation (wavelet coefficients).

Three different cases have been considered, which are summarised in Table 2. Case A actually corresponds to the simulations studied in the previous sections, for which all six components were kept in the equations. The outcome of the computations is presented in Fig. 16. A fourth configuration was tested in which all the contributions, except for D_0^P, were removed. This led to divergence of the solution. It appears that some drain of energy must exist at the end of the energy cascade. In a multilevel LES, this end is placed at the highest resolution level considered, i.e. $\mathbf{W}_{j+1}$ for a two-level simulation. Ignoring the dissipation term D_2^Q will lead to energy pile-up at the highest wavenumber and the emergence of instabilities in the solution. The results shown in these plots suggest that in case *LES-Lo2* the best candidate for a simplified version of the equations is configuration *B*, in which the viscous SGS term, D_0^Q, is removed in (57), together with the large-scale component, D_1^P, in (58), and D_2^P, in (59). Configuration *C* provided slightly poorer results, which indicates that, at this lower Reynolds num-

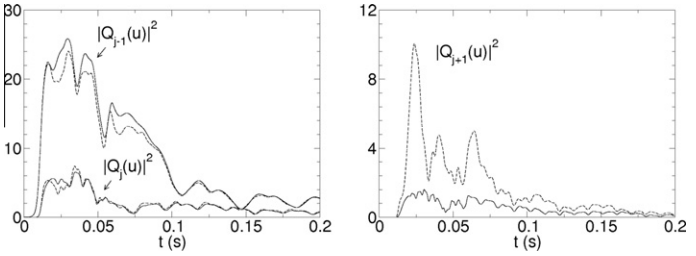

Fig. 15. [Re = 15,000] Time evolution of the variance of the wavelet coefficients for the LES Burgers equation ($J = 15$, $j = 7$, $M = 2$). Level $j-1$: $|Q_{j-1}(u)|^2$, level j: $|Q_j(u)|^2$, and level $j+1$: $|Q_{j+1}(u)|^2$ (– DNS; –– LES).

Table 2
Configurations to investigate the effect of the viscous SGS terms.

Case	D_0^P	D_0^Q	D_1^P	D_1^Q	D_2^P	D_2^Q
A	1	1	1	1	1	1
B	1	0	0	1	0	1
C	1	0	0	0	0	1

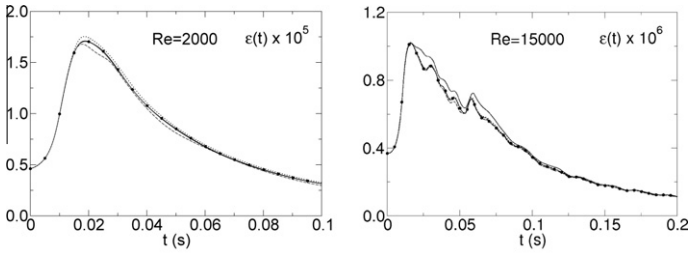

(a) $Re = 2000,\ LES - Lo2$ (b) $Re = 15000,\ LES - Hi2$

Fig. 16. Study of the viscous SGS terms. Time evolution of total dissipation, $\varepsilon(t)/15\nu$, for the LES Burgers equation (– DNS; –•– LES Case A; ··· LES Case B; – – LES Case C).

Table 3
CPU times of the LES and the full DNS simulations.

Simulation	*Re*	Δt	CPU time
DNS-Lo	2000	10^{-5}	10 min, 49 s
LES-Lo1-B	2000	10^{-4}	63 s
LES-Lo2-B	2000	10^{-4}	148 s
DNS-Hi	15,000	10^{-6}	1 day, 12 h
LES-Hi2-C	15,000	10^{-4}	243 s

ber, an important part of the energy dissipation takes place in $\mathbf{W}_j$. For the high-Reynolds-number simulation *LES-Hi2*, all three configurations led to similarly good results, which is a manifestation that most of the dissipation occurs at the finest scales.

Table 3 compares the CPU times of the LES, for the simplified cases B at Re = 2000 and C at Re = 15,000, and the full DNS. The total run time was 5 initial eddy-turnover times for the low Reynolds number, and 10 initial eddy-turnover times for the high Reynolds number simulations. We can appreciate a significant reduction of the computational effort in the LES with respect to DNS, partly due to the larger time steps allowed in these simulations.

6.4. Force-driven Burgers turbulence

This section represents a complement to Sections 6.1 and 6.2. Its purpose is to demonstrate that our wavelet-based approach is also stable under the action of a random force.

The forced Burgers equation reads

$$\frac{\partial u}{\partial t} + \frac{\partial}{\partial x}\left(\frac{u^2}{2}\right) - \frac{1}{Re}\frac{\partial^2 u}{\partial x^2} = f(x,t) \tag{60}$$

where $f(x,t)$ represents the forcing term in physical space. In this research, we have adopted the simple white-in-time random forcing used by Chekhlov and Yakhot in their studies on Kolmogorov turbulence [34]. In Fourier space, this force is defined as $\hat{f}(\kappa,t) = A_f/\sqrt{\Delta t}\mid\kappa\mid^{-1/2}\sigma_\kappa$, where A_f is a constant, Δt is the time step, and σ_κ is a Gaussian random variable with Normal distribution $\mathcal{N}(0,1)$. We call κ_c the force cut-off, such that $\hat{f}(\kappa,t) = 0$ for $\kappa > \kappa_c$. Note that the uncorrelated nature of this random force will not affect whatsoever the conclusions from these analyses. In fact, we are only interested in studying the dynamical behaviour of the proposed numerical method and not in the specific statistical properties of the solution.

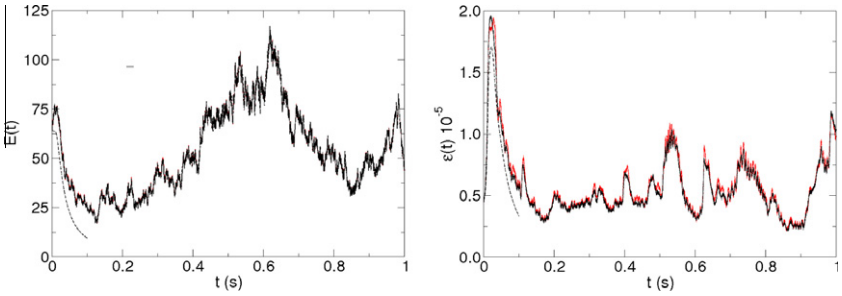

Fig. 17. [*LES-Lo1-B*] Solution of the forced Burgers LES equation ($A_f = 5.0$, $\kappa_c = 8$). Time evolution of total energy $E(t)$ (left) and dissipation, $\varepsilon(t)/15\nu$ (scaled by a factor of 10^{-5}) (right). In both graphs: (black, forced DNS; red, forced LES; black —- decaying LES). (For interpretation of the references to colour in this figure legend, the reader is referred to the web version of this article.)

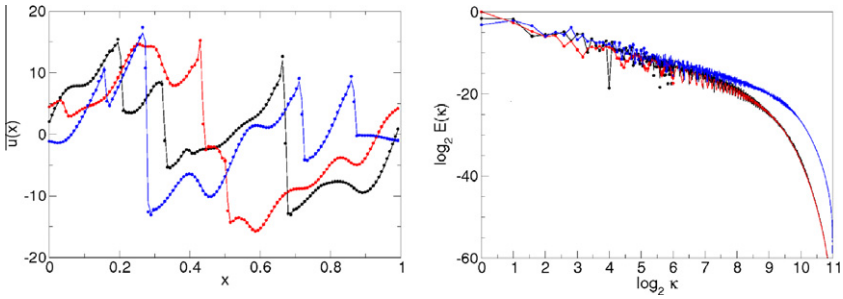

Fig. 18. [*LES-Lo1-B*] Solution of the LES forced Burgers equation ($A_f = 5.0$, $\kappa_c = 8$). Velocity profiles (left) and energy spectra (right) at different instants of time (black, $t = 0.4$ s, red, $t = 0.6$ s, blue, $t = 1$ s; – DNS, •LES). (For interpretation of the references to colour in this figure legend, the reader is referred to the web version of this article.)

The application of the force at each time step is done by transforming the LES solution into Fourier space and by adding $\hat{f}(\kappa, t)$ to all modes below the cut-off. Based on the conclusions drawn from the previous section, we have selected configurations *LES-Lo1-B* and *LES-Hi2-C* to carry out these tests. Despite the simplifications introduced (some of the diffusion terms in the small-scale equations were neglected), both configurations proved to provide accurate results in the case of decaying Burgers turbulence, and represent the worst case scenario. The initial solution is the same one used in those tests. In order to compare the results from the LES simulations against the projected DNS, we use in all cases the same *seed* for the random number generator [31], as well as the same time step which is determined by the DNS (see Table 3). The parameter A_f is tuned so that a high level of energy is continuously injected at wavenumbers smaller or equal than $\kappa_c = 8$. For the case $Re = 2000$ we set $A_f = 5.0$, and for the case $Re = 15{,}000$ we have $A_f = 14.1$.

The results from these calculations are shown in Figs. 17–20. Figs. 17 and 19 compare the time evolution of the large-scale energy and dissipation for both configurations. The time evolution of energy in the case of decaying Burgers turbulence is also shown for comparison (dashed line). These plots show that the forcing term was able to keep a high level of energy throughout the whole simulation. Besides, the random character of this term ensures that the simulation progresses through very different stages, in which the energy is either growing or decaying, and at all times fluctuating. The values of the LES

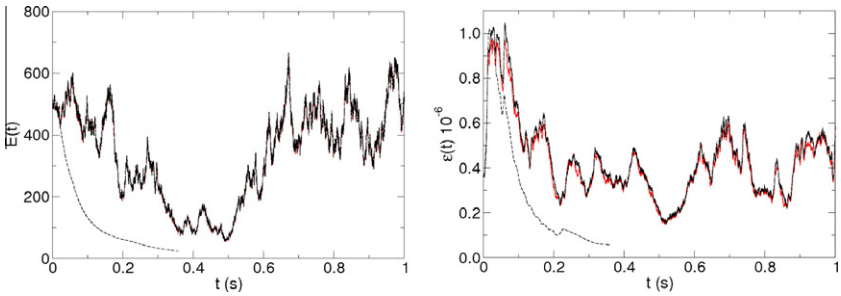

Fig. 19. [*LES-Hi2-C*] Solution of the forced Burgers LES equation ($A_f = 14.1$, $\kappa_c = 8$). Time evolution of total energy $E(t)$ (left) and dissipation, $\varepsilon(t)/15\nu$ (scaled by a factor of 10^{-6}) (right). In both graphs: (black, forced DNS; red, forced LES; black –- decaying LES). (For interpretation of the references to colour in this figure legend, the reader is referred to the web version of this article.)

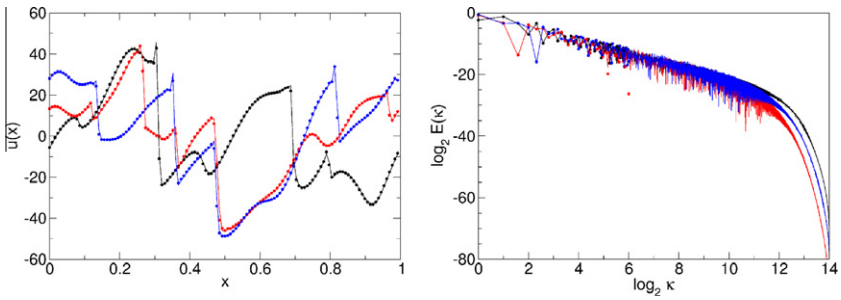

Fig. 20. [*LES-Hi2-C*] Solution of the LES forced Burgers equation ($A_f = 14.1$, $\kappa_c = 8$). Velocity profiles (left) and energy spectra (right) at different instants of time (black, $t = 0.15$ s, red, $t = 0.65$ s, blue, $t = 0.95$ s; – DNS, •LES). (For interpretation of the references to colour in this figure legend, the reader is referred to the web version of this article.)

large-scale energy and dissipation also appear very close to those of the projected DNS solution. This is specially so for the evolution of energy, for which the differences between LES and DNS are almost imperceptible.

Figs. 18 and 20 compare the velocity profiles and the energy spectra of the LES simulation against the DNS at three different time instants during the simulation in which the solution contained a high level of energy. Observe that the LES simulation is able to capture with high fidelity the large-scale structure of the solution, presenting only some discrepancies near the shocks. This is in agreement with the results of Sections 6.1 and 6.2. Once more, the LES and DNS energy spectra are in good agreement.

7. Conclusions

A systematic approach to the solution of the LES equations has been developed based on the MRA technique. This methodology provides a consistent mathematical framework for the decomposition of the flow into large and small scales, and gives deep insight into the physics of the turbulent cascade. Furthermore, because of the inherent sparseness of the wavelet representation, this approach naturally lends itself to the implementation of spatio-temporal adaptive schemes [35].

Based on this formalism, the LES equations have been derived for the particular cases of the 1D Burgers equation and the 3D incompressible N–S equations. The projection of the equations on the LES grid gives rise to a series of closure terms. These terms can be calculated directly as a function of the wavelet coefficients, which are known from the solution of the small-scale equations on the wavelet spaces. A pressure SGS term also arises whose role is to enforce the continuity condition on the LES grid. A standard pressure-correction method may be used to this end.

The wavelet-based LES technique has been assessed in *a priori* tests on an atmospheric turbulence data set from experiment, and on homogeneous isotropic turbulence from DNS. The outcome of these tests demonstrates the accuracy of the method in representing the convective SGS component through a truncated wavelet expansion of the velocity field. Moreover, it suggests that a good level of approximation can be achieved even when only one term is considered in the series.

A posteriori tests on decaying and force-driven Burgers turbulence have been carried out at high (equivalent) Reynolds numbers. The simulations were able to reproduce relatively well the solution in the vicinity of the shocks. Good agreement between the LES and the projected DNS solution was also found for the energy spectrum, as well as for the time evolution of the total energy and total dissipation.

The relative importance of the viscous SGS term in the large-scale Burgers equation with respect to the convective SGS term has also been investigated *a posteriori*. The findings corroborate the conclusions drawn from the *a priori* analyses, i.e. the effect of subgrid diffusion in the coarse-scale equation may be safely neglected. From these observations, it appears very likely that this will also be case in 3D turbulence. However, only the actual implementation and verification of these assumptions in the 3D N–S problem will answer this question.

The results from these investigations appear very encouraging and therefore demonstrate the potential of our approach as a powerful alternative to traditional LES. They also highlight the virtues of the WT as an effective tool for the numerical simulation of turbulent flows.

The first step to take in the continuation of this work is therefore to develop an efficient coding strategy for the solution of the 3D LES N–S equations. For this purpose, there exist in the literature fast algorithms for the WT, as well as for the derivation and multiplication of functions in wavelet bases (see e.g. the work of Beylkin et al. [36], and Beylkin and Keiser [23]). The final implementation should incorporate an adaptive strategy able to exploit the sparseness property of the wavelet representation.

Taking into account that engineering problems of practical importance often involve the specification of realistic boundary conditions and irregular grids, it is also important to envision the extension of the methodology to non-periodic domains. The second generation wavelets (SGW) developed by Sweldens [37] might serve this purpose. SGW provide greater flexibility and therefore are able to deal with a broader range of applications. Moreover, fast algorithms for the efficient implementation of their associated WT are available in the literature [38].

Finally, an attractive avenue for future work is the application of this methodology to the solution of turbulent reacting flows. Note that in the case of compressible flows, the mass conservation problem mentioned above is avoided. However, the compressible character of this type of flow, and obviously the complex chemistry involved, will pose new challenges which should be carefully investigated.

Acknowledgements

The authors thank R. Prosser and A.J. Lowe for useful discussions. This research has been funded by the UK Engineering and Physical Sciences Research Council, with additional support from Zonta International through the Amelia Earhart fellowship program.

Appendix A. Clarification note

The aim of this appendix is to clarify the differences between the proposed methodology and the SCALES approach [17,18] introduced in Section 1.

For the purpose of this appendix, and in order to make the discussion more fluid, we will refer to the approach presented in this paper as WaveLES.

Let us start by recalling that SCALES is based on a combination of the CVS technique and the Germano dynamic approach. The reduction in the number of degrees of freedom in SCALES, as well as in CVS, is achieved by non-linear filtering the solution using wavelet thresholding. In WaveLES, the reduction in the number of degrees of freedom with respect to DNS is accomplished thanks to two different operations. Firstly, the wavelet series (MRA) of the solution is truncated at a prescribed level, say M (usually $M = 1$ or $M = 2$). Secondly, non-linear filtering is applied to the retained wavelet spaces by setting the value of the threshold ϵ to a specified level. As an example, in SCALES, or in CVS, we could have a grid point that belongs to the wavelet space $\mathbf{W}_{J-1}$, representative of the smallest scales resolved in a DNS, given that the value of its associated coefficient is above the threshold. By contrast, in WaveLES, the smallest scales accounted for in the simulation live in the space $\mathbf{W}_m$, where m is the maximum level considered in the simulation, which in the case of a one-level approach corresponds to $m = j$, i.e. $\mathbf{W}_j$.

There is another important difference between both methods, which does not appear obvious in the case of the 1D Burgers problem. However, we will see that this difference manifests clearly in the case of the 3D N–S problem. Remember that in SCALES the SGS stresses are modelled using a dynamic eddy viscosity model based on the Germano procedure. The value of the model constant is then calculated dynamically by using two levels of the wavelet filter. By contrast, in WaveLES, the convective SGS terms (27) in the large-scale momentum equations are approximated using the available information of the small scales. This information is obtained by explicitly solving a simplified version of the small-scale equations on the subspaces $\mathbf{W}_m$. Although the actual implementation of the 3D problem has not yet been carried out, we believe that a number of reasonable assumptions can be made in order to reduce the complexity of the problem. These are outlined below,

(1) As already explained in Section 4.5, it is sensible to neglect the pressure term on the small-scale Eq. (39). Based on the same grounds, we may also ignore the contribution of the pressure SGS term (35) to the resolved field.
(2) As has been shown in Section 5, *a priori* studies carried out on homogeneous isotropic turbulence have lead to the conclusion that the viscous SGS terms (34) that appear in the large-scale momentum equation are negligible with respect to their convective counterpart. *A posteriori* tests performed on the Burgers equation (see Section 6) have shown that additional diffusion terms can be safely removed from the small-scale equations, namely the terms $\nu Q_m \partial^2/\partial x^2 P_m(u)$, for $m = j, \ldots, j + M - 1$. Although, it is still premature to extrapolate these findings to the practical implementation of the 3D problem, common knowledge of the physics of the turbulent cascade suggests that this may well be the case.
(3) As discussed in Section 4.7 the treatment of the continuity equation may be further simplified by ignoring the effects of the mass conservation SGS term (36) in the continuity Eq. (26). This is standard practice in LES. Indeed, most LES approaches ignore the fact that the application of a spatial filter to the continuity equation will generate commutation errors, unless the filter is commutative with the derivative operation.

Note as well that in SCALES, the LES equations are advanced in the physical domain, whereas in WaveLES the system of equations is solved in wavenumber space directly, only returning to physical space for the calculation of the non-linear terms (pseudo-wavelet approach). However, should future investigations show that it is computationally more efficient to solve the equations in physical space, the methodology could be straightforwardly reformulated to this end.

In this sense, WaveLES is closer in spirit to the multilevel LES methods presented in [1,5] or [8], for example, with the novelty that the wavelet basis provides a natural framework for the scale separation problem, and the implementation of adaptive schemes.

Finally, we are aware that in the solution of practical problems it may be necessary to supplement the small-scale equations with an additional dissipation term. This new term will account for the effect of the discarded modes (those at levels $m > j + M - 1$) on the resolved field, and will ensure that a sufficient amount of dissipation is taking place during runtime. This is a strategy very often used in multilevel LES methods. More specifically, in VMS [8], the small-scale equations usually entail very simple models, such as the Smagorinsky closure, whereas no explicit modelling term is included in the equations for the large scales. It is this same strategy that we would certainly use in a 3D WaveLES, and not the application of a global (in scale) model to the LES solution, as is done in SCALES.

References

[1] P.R. Voke, Multiple mesh simulation of turbulence, in: K.W. Morton, M.J. Baines (Eds.), Proc. Numer. Methods Fluid Dyn. III, 1988, pp. 333–340.
[2] P.R. Voke, Multiple Mesh Simulation of Turbulent Flow, Technical Report, QMW EP-1082, University of London, 1990.
[3] M. Terracol, P. Sagaut, C. Basdevant, A multilevel algorithm for LES of turbulent compressible flows, J. Comput. Phys. 167 (2001) 429–474.
[4] M. Terracol, P. Sagaut, C. Basdevant, A time self-adaptive multilevel algorithm for large-eddy simulation, J. Comput. Phys. 184 (2003) 339–365.
[5] J.A. Domaradzki, P.P. Yee, The subgrid-scale estimation model for high Reynolds number turbulence, Phys. Fluids 12 (2000) 193–196.
[6] J.M. McDonough, J.C. Bywater, R.J. Buell, An investigation of strange attractor theory and small-scale turbulence, in: Proc. 17th AIAA Fluid Dyn. Plasma Dyn. Lasers Conf. Paper 84-1674, Snowmass, CO, June 1984.
[7] J.M. McDonough, J.C. Bywater, R.J. Buell, A comparison of routes to a strange attractor in one-dimensional local models of turbulent free and forced convection, in: Proc. ASME Winter Annu. Meet., New Orleans, LA, Paper 84-WA/HT-16, December 1984.
[8] T.J.R. Hughes, L. Mazzei, A.A. Oberai, A.A. Wray, The multiscale formulation of large-eddy simulation: decay of homogeneous isotropic turbulence, Phys. Fluids 13 (2001) 505–512.
[9] T.J.R. Hughes, A.A. Oberai, L. Mazzei, Large-eddy simulation of turbulent channel flows by the variational multiscale method, Phys. Fluids 13 (2001) 1784–1799.

[10] J. Liandrat, P. Tchamitchian, Resolution of the 1D Regularised Burgers Equation using a Spatial Wavelet Approximation, NASA, ICASE Report, 1990.
[11] E. Bacry, S. Mallat, G. Papanicolaou, A wavelet based space–time adaptive numerical method for partial differential equations, Math. Model. Numer. Anal. 26 (1992) 793–834.
[12] C. Meneveau, Analysis of turbulence in the orthogonal wavelet representation, J. Fluid. Mech. 232 (1991) 469–520.
[13] M. Farge, Wavelet transforms and their application to turbulence, Annu. Rev. Fluid Mech. 24 (1992) 395–457.
[14] M. Farge, K. Schneider, N.K.-R. Kevlahan, Non-Gaussianity and coherent vortex simulation for two-dimensional turbulence using an adaptive orthogonal wavelet basis, Phys. Fluids 11 (1999) 2187–2201.
[15] R. Prosser, R.S. Cant, On the use of wavelets in computational combustion, J. Comput. Phys. 147 (1998) 337–361.
[16] H. Bockhorn, J. Fröhlich, K. Schneider, An adaptive two-dimensional wavelet-vaguelette algorithm for the computation of flame balls, Combust. Theory Model 3 (1999) 177–198.
[17] D.E. Goldstein, O.V. Vasilyev, Stochastic coherent adaptive large eddy simulation method, Phys. Fluids 16 (2004) 2497–2513.
[18] D.E. Goldstein, O.V. Vasilyev, N.K.-R. Kevlahan, CVS and SCALES simulation of 3-D isotropic turbulence, J. Turbul. 6 (2005) 37.
[19] M. Germano, U. Piomelli, P. Moin, W.H. Cabot, A dynamic subgrid-scale eddy-viscosity model, Phys. Fluids A 3 (1991) 1760–1765.
[20] S. Mallat, A theory for multiresolution signal decomposition: the wavelet representation, IEEE Trans. Pattern Anal. Mach. Intell. 11 (1989) 674–693.
[21] S. Mallat, A Wavelet Tour of Signal Processing, Academic Press, 1998.
[22] I. Daubechies, Ten Lectures on Wavelets, SIAM, Philadelphia, Pennsylvania, 1992.
[23] G. Beylkin, J.M. Keiser, On the representation of operators in bases of compactly supported wavelets, J. Comput. Phys. 132 (1997) 233–259.
[24] G.S. Winckelmans, D. Carati, H. Jeanmart, On the comparison of turbulence intensities from large-eddy simulation with those from experiment or direct numerical simulation, Phys. Fluids 14 (2002) 1809–1811.
[25] T.S. Lund, The use of explicit filters in large-eddy simulation, Comp. Math. Appl. 46 (2003) 603–616.
[26] G. De Stefano, O.V. Vasilyev, Perfect modeling framework for dynamic subgrid-scale model testing in large-eddy simulation, Theor. Comput. Fluid Dyn. 18 (2004) 27–41.
[27] B.J. Geurts, D.D. Holm, Commutator errors in large-eddy simulation, J. Phys. A: Math. Gen. 39 (2006) 2213–2229.
[28] <http://www2.isye.gatech.edu/brani/datapro.html>.
[29] R.H. Kraichnan, Eddy viscosity in two and three dimensions, J. Atmos. Sci. 83 (1976) 1521–1536.
[30] J.A. Domaradzki, W. Liu, M.E. Brachet, An analysis of subgrid-scale interactions in numerically simulated isotropic turbulence, Phys. Fluids A 5 (1993) 1747–1759.
[31] R.S. Cant, FERGUS: A User Guide, Technical Report, Cambridge University Engineering Department, 1999.
[32] M. de la Llave Plata, The Application of Wavelets to LES Modelling of Turbulent Flows, Ph.D. Thesis, University of Cambridge, November 2007.
[33] R.S. Cant, Initial Conditions for Direct Numerical Simulation of Turbulence, Technical Report, CUED-THERMO-2001/01, Cambridge University, 2001.
[34] A. Chekhlov, V. Yakhot, Kolmogorov turbulence in a random-force-driven Burgers equation, Phys. Rev. E 51 (1995) 2739–2742.
[35] J.M. Alam, N.K.-R. Kevlahan, O.V. Vasilyev, Simultaneous space–time adaptive wavelet solution of nonlinear parabolic differential equations, J. Comput. Phys. 214 (2006) 829–857.
[36] G. Beylkin, R. Coifman, V. Rokhlin, Fast wavelet transforms and numerical algorithms I, Commun. Pure Appl. Math. 44 (1991) 141–183.
[37] W. Sweldens, The Lifting Scheme: A New Philosophy in Biorthogonal Wavelet Constructions, in: A.F. Laine, M. Unser (Eds.) Proc. SPIE 2569, Wavelet Applications in Signal and Image Processing III, 1995, pp. 68–79.
[38] P. Schröder, W. Sweldens, Building your own wavelets at home, ACM SIGGRAPH Course Notes, 1996.